Supporting Information for

Eu^{3+}/Tb^{3+}-modified Cd(II) coordination polymers for effective detection of uric acid and lung cancer biomarker *N*-acetylneuraminic acid

Hongjian Li[a], Yuqian Chen[a], Hengyi Zhao[a], Huiqi Zou[a], Hui Yan[b], Jing Lu[a], Hongguo Hao[a], Jianmin Dou[a], Yunwu Li[a*], Suna Wang[a*]

[a] Shandong Provincial Key Laboratory of Chemical Energy Storage and Novel Cell Technology, School of Chemistry and Chemical Engineering, Liaocheng University, Liaocheng, 252059, People's Republic of China.

[b] School of Pharmacy, Liaocheng University, Liaocheng, 252059, People's Republic of China.

Email: wangsuna@lcu.edu.cn; liyunwu@lcu.edu.cn

Table of Contents

Table S1. Crystal structure data and refinement parameters of **Cd-CP2**.

Table S2. Selected bond lengths [Å] and angles [º] for **Cd-CP2**.

Table S3. Comparison of detection capacities of **Cd-CP2** toward UA with other probes.

Fig. S1. PXRD of as-synthesized **Cd-CP2**, **Eu^{3+}@Cd-CP2** and **Tb^{3+}@Cd-CP2**.

Fig. S2. (a) FT-IR spectra of the H_3L**, Cd-CP2** and **Eu^{3+}@Cd-CP2**. (b) FT-IR spectra of H_3L, **Cd-CP2** and **Tb^{3+}@Cd-CP2**.

Fig. S3. (a-c) SEM of **Cd-CP2**, **Eu^{3+}@Cd-CP2** and **Tb^{3+}@Cd-CP2**. (d-f) 2D AFM image of **Cd-CP2**, **Eu^{3+}@Cd-CP2** and **Tb^{3+}@Cd-CP2**. (g-i) 3D AFM image of **Cd-CP2**, **Eu^{3+}@Cd-CP2** and **Tb^{3+}@Cd-CP2**.

Fig. S4. (a) EDS mapping results of **Eu^{3+}@Cd-CP2**. (b) EDS mapping results of **Tb^{3+}@Cd-CP2**.

Fig. S5. (a) XPS spectra of **Cd-CP2** and **Eu^{3+}@Cd-CP2**. (b) C1s XPS, (c) N1s XPS, (d) O1s XPS, (e) Cd3d XPS, and (f) Eu3d XPS spectra of **Cd-CP2** and **Eu^{3+}@Cd-CP2**.

Fig. S6. (a) XPS spectra of **Cd-CP2** and **Tb^{3+}@Cd-CP2**. (b) C1s XPS, (c) N1s XPS, (d) O1s XPS, (e) Cd3d XPS, and (f) Tb3d XPS spectra of **Cd-CP2** and **Tb^{3+}@Cd-CP2**.

Fig. S7. Luminescence spectra and photos of aqueous suspensions of **Cd-CP2**, **Eu^{3+}@Cd-CP2**, **Tb^{3+}@Cd-CP2** under 254 nm UV light.

Fig. S8. (a-c) PXRD of **Cd-CP2**, **Eu^{3+}@Cd-CP2** and **Tb^{3+}@Cd-CP2** after being immersed in H_2O for different time.

Fig. S9. (a) Emission spectra of **Cd-CP2** after being immersed in H_2O for different time; (b) The corresponding intensity histogram diagram of $I_{350\ nm}$.

Fig. S10. (a) Emission spectra of **Eu^{3+}@Cd-CP2** after being immersed in H_2O for different time; (b) The corresponding intensity histogram diagram of $I_{355\ nm}$ and $I_{615\ nm}$.

Fig. S11. (a) Emission spectra of **Tb^{3+}@Cd-CP2** after being immersed in H_2O for different time; (b) The corresponding intensity histogram diagram of $I_{355\ nm}$ and $I_{545\ nm}$.

Fig. S12. (a-c) PXRD of **Cd-CP2**, **Eu^{3+}@Cd-CP2** and **Tb^{3+}@Cd-CP2** after being immersed in the solutions of pH = 4-9.

Fig. S13. (a) The emission spectra of **Cd-CP2** after immersing in aqueous solutions with different pH values. (b) The photo of **Cd-CP2** in different pH values irradiated by 254 nm UV lamp. (c) The emission spectra of **Eu^{3+}@Cd-CP2** after immersing in aqueous solutions with different pH values. (d) The photo of **Eu^{3+}@Cd-CP2** in different pH values irradiated by 254 nm UV lamp. (e) The emission spectra of **Tb^{3+}@Cd-CP2** after immersing in aqueous solutions with different pH values. (f) The

photo of **Tb^{3+}@Cd-CP2** in different pH values irradiated by 254 nm UV lamp.

Fig. S14. TG of **Cd-CP2, Eu^{3+}@Cd-CP2, Tb^{3+}@Cd-CP2**.

Fig. S15. The detection limit calculation of **Cd-CP2 (**10^{-3} M**)** towards UA based on the intensity of 350 nm.

Fig. S16. Luminescence intensities of **Cd-CP2** toward other urine components with and without UA based on the intensity at 350 nm.

Fig. S17. (a-i) The luminescence emission of **Cd-CP2** toward other urine components with and without UA.

Fig. S18. Response time of **Cd-CP2** toward UA based on the intensity at 350 nm.

Fig. S19. The repeatability of **Cd-CP2** in sensing of UA based on the intensity at 350 nm within five cycles.

Fig. S20. PXRD of **Cd-CP2** after being immersed in UA solutions (10^{-3} M).

Fig. S21. The luminescence lifetime decay curves of **Cd-CP2** and **Cd-CP2** with UA.

Fig. S22. The calculated HOMO and LUMO energy levels of H_3L and UA.

Fig. S23. UV−vis absorption spectra of various urine chemicals and excitation of **Cd-CP2**.

Fig. S24. (a) XPS of **Cd-CP2** before and after immersing in 10^{-3} M UA aqueous solutions. (b) C1s XPS, (c) N1s XPS, (d) O1s XPS and (e) Cd3d XPS of **Cd-CP2** before and after immersing in 10^{-3} M UA aqueous solutions.

Fig. S25. (a) Luminescence titration of **Eu^{3+}@Cd-CP2** toward UA in the low concentration range. (b) Luminescence titration of **Tb^{3+}@Cd-CP2** toward UA in the low concentration range.

Fig. S26. (a) The detection limit calculation of **Eu^{3+}@Cd-CP2** towards NANA based on the intensity at 615 nm. (b) The detection limit calculation of **Tb^{3+}@Cd-CP2** towards NANA based on the intensity at 545 nm.

Fig. S27. (a-i) The luminescence emission of **Eu^{3+}@Cd-CP2** toward other urine components with and without NANA.

Fig. S28. (a-i) The luminescence emission of **Tb^{3+}@Cd-CP2** toward other urine components with and without NANA.

Fig. S29. (a) Response time of **Eu^{3+}@Cd-CP2** toward NANA based on the intensity at 615 nm. (b) Response time of **Tb^{3+}@Cd-CP2** toward NANA based on the intensity at 545 nm.

Fig. S30. (a) The repeatability of **Eu^{3+}@Cd-CP2** based on the intensity at 545 nm in sensing of NANA. (b) The repeatability of **Tb^{3+}@Cd-CP2** based on the intensity at 545

nm in sensing of NANA.

Fig. S31. (a-c) PXRD of **Cd-CP2**, **Eu^{3+}@Cd-CP2** and **Tb^{3+}@Cd-CP2** after being immersed in the solutions of synthetic urine or HEPES buffer solution (pH = 7.0).

Fig. S32. (a-b) Luminescence titration result of **Cd-CP2** toward UA in synthetic urine and HEPES buffer solution (pH = 7.0). (c-d) Luminescence titration result of **Eu^{3+}@Cd-CP2** toward NANA in synthetic urine and HEPES buffer solution (pH = 7.0). (e-f) Luminescence titration result of **Tb^{3+}@Cd-CP2** toward UA in synthetic urine and HEPES buffer solution (pH = 7.0).

Fig. S33. Fluorescence spectra of different concentrations of NANA and photographs under 254 nm UV lamps.

Fig. S34. (a) PXRD of **Eu^{3+}@Cd-CP2** after being immersed in the solutions of NANA. (b) PXRD of **Tb^{3+}@Cd-CP2** after being immersed in the solutions of NANA.

Fig. S35. (a) UV−vis absorption spectra of various urine chemicals and excitation spectra of **Eu^{3+}@Cd-CP2**. (b) UV−vis absorption spectra of various urine chemicals and excitation spectra of **Tb^{3+}@Cd-CP2**.

Fig. S36. The calculated HOMO and LUMO energy levels of H_3L and NANA.

Fig. S37. (a) XPS of **Eu^{3+}@Cd-CP2** before and after immersing in 10^{-3} M NANA aqueous solutions. (b) C1s XPS, (c) N1s XPS, (d) O1s XPS, (e) Cd3d XPS, and (f) Eu3d XPS of **Eu $^{3+}$@Cd-CP2** before and after immersing in 10^{-3} M NANA aqueous solutions.

Fig. S38. (a) XPS of **Tb^{3+}@Cd-CP2** before and after immersing in 10^{-3} M NANA aqueous solutions. (b) C1s XPS, (c) N1s XPS, (d) O1s XPS, (e) Cd3d XPS, and (f) Td3d XPS of **Tb^{3+}@Cd-CP2** before and after immersing in 10^{-3} M NANA aqueous solutions.

Fig. S39. Simplified schematic diagram of the energy transfer from the ligand to Eu^{3+} and Tb^{3+} ions and the mechanism of luminescence quenching.

Fig. S40. (a) The luminescence lifetime decay curves of $I_{355\ nm}$ of **Eu^{3+}@Cd-CP2** and **Eu^{3+}@Cd-CP2** with NANA. (b) The luminescence lifetime decay curves of $I_{615\ nm}$ of **Eu^{3+}@Cd-CP2** and **Eu^{3+}@Cd-CP2** with NANA. (c) The luminescence lifetime decay curves of $I_{355\ nm}$ of **Tb^{3+}@Cd-CP2** and **Tb^{3+}@Cd-CP2** with NANA. (d) The luminescence lifetime decay curves of $I_{545\ nm}$ of **Tb^{3+}@Cd-CP2** and **Tb^{3+}@Cd-CP2** with NANA.

Fig. S41. Photos of the mixture of H_3L, **Cd-CP2** and Eu^{3+} or Tb^{3+} as well as **Eu^{3+}@Cd-CP2** and **Tb^{3+}@Cd-CP2** with or without NANA (10^{-3} M) under 254 nm UV light.

Materials and characterization.

Powder X-ray diffraction (PXRD) data were collected over the 2θ range of 5–50° using a SmartLab diffractometer with Cu Kα radiation (λ=1.5418 Å) at room temperature. The FT-IR spectra (4000-400 cm^{-1} region) were recorded from KBr pellets with a NICOLET 6700F-IR spectrometer. Thermal analyses were performed on STA 449 F5 Jupiter instrument from room temperature to 800°C with a heating rate of 10°C/min under flowing nitrogen. Emission and excitation spectra in solid state as well as lifetime luminescence were carried out on a FLS1000 spectrophotometer analyzer of Edinburgh instruments. Luminescence sensing properties were recorded on the Hitachi F-7000 Luminescence spectrophotometer. X-ray photoelectron spectroscopy (XPS) characterization was carried out by using a Thermo Fisher Scientific ESCALAB Xi+ spectrometer with Al Kα X-rays (1486.6 eV). UV-vis measurements were conducted with a UH 4150 spectrophotometer. The SEM and EDS mapping were recorded with FIB Helios G4. The inductively coupled plasma mass spectrometer (ICP) were recorded with ThermoFisher iCAPRQ. The AFM were recorded with Multimode8 Solver P47.

X-ray crystallographic study.

Single-crystal X-ray data for **Cd-CP2** were collected on a Siemens Smart CCD diffractometer with graphite-monochromatic Mo Kα radiation (λ = 0.71073 Å) at 298 K. The raw data frames were integrated into SHELX-format reflection files and corrected using SAINT program. Absorption corrections based on multi-scan were obtained by the SADABS program. The structure was solved with direct methods (SHELXS) and refined with full-matrix least-squares technique using the SHELXL-2018/3 programs. Displacement parameters were refined anisotropically, and the positions of the H-atoms were generated geometrically, assigned isotropic thermal parameters, and allowed to ride on their parent carbon atoms before the final cycle of refinement. Basic information pertaining to crystal parameters and structure refinement is summarized in Table S1. Selected bond lengths and angles are listed in Table S2.

Calculation of the HOMO and LUMO.

The HOMO–LUMO energy levels were calculated at the b3pw91/6-31g accuracy level by density functional theory (DFT), using the Gaussian 16 package of programs. The harmonic frequency was calculated to make sure that the acquired structure was the local minimum.

Gaussian 16, Revision C.01, Frisch, M. J.; Trucks, G. W.; Schlegel, H. B.; Scuseria, G. E.; Robb, M. A.; Cheeseman, J. R.; Scalmani, G.; Barone, V.; Petersson, G. A.;

Nakatsuji, H.; Li, X.; Caricato, M.; Marenich, A. V.; Bloino, J.; Janesko, B. G.; Gomperts, R.; Mennucci, B.; Hratchian, H. P.; Ortiz, J. V.; Izmaylov, A. F.; Sonnenberg, J. L.; Williams-Young, D.; Ding, F.; Lipparini, F.; Egidi, F.; Goings, J.; Peng, B.; Petrone, A.; Henderson, T.; Ranasinghe, D.; Zakrzewski, V. G.; Gao, J.; Rega, N.; Zheng, G.; Liang, W.; Hada, M.; Ehara, M.; Toyota, K.; Fukuda, R.; Hasegawa, J.; Ishida, M.; Nakajima, T.; Honda, Y.; Kitao, O.; Nakai, H.; Vreven, T.; Throssell, K.; Montgomery, J. A., Jr.; Peralta, J. E.; Ogliaro, F.; Bearpark, M. J.; Heyd, J. J.; Brothers, E. N.; Kudin, K. N.; Staroverov, V. N.; Keith, T. A.; Kobayashi, R.; Normand, J.; Raghavachari, K.; Rendell, A. P.; Burant, J. C.; Iyengar, S. S.; Tomasi, J.; Cossi, M.; Millam, J. M.; Klene, M.; Adamo, C.; Cammi, R.; Ochterski, J. W.; Martin, R. L.; Morokuma, K.; Farkas, O.; Foresman, J. B.; Fox, D. J. Gaussian, Inc., Wallingford CT, 2016.

Table S1. Crystal structure data and refinement parameters of **Cd-CP2**.

Cd-CP2			
Formula	$C_{35}H_{30}N_2O_9Cd$	V [Å^3]	3105.14(17)
formula weight	735.01	Z	4
T (K)	293(2)	ρ_{calc} [g·cm^{-3}]	1.572
Crystal system	Monoclinic	μ [mm^{-1}]	6.151
Space group	$P2_1/n$	θ range	3.858-71.193
a [Å]	11.6644(3)		-14<=h<=11,
b [Å]	22.9153(6)	index ranges	-28<=k<=28,
c [Å]	12.4762(4)		-15<=l<=14
α [˚]	90	R1;wR_{2a} [I> 2σ(I)]	0.0377, 0.0843
β [˚]	111.388(4)	GOF	1.032
γ [˚]	90	R1;wR_{2a} [all data]	0.0387, 0.0872

$^aR_1 = \Sigma| |F_o|-|F_c| |/ \Sigma|F_o|$, $^bwR_2 = [\Sigma w(F_o^2-F_c^2)^2]/ \Sigma w(F_o^2)^2]^{1/2}$

Table S2. Selected bond lengths [Å] and angles [º] for **Cd-CP2**.

Cd(1)-O(1)	2.279(2)	Cd(1)-O(2)	2.604(3)
Cd(1)-N(1)	2.336(3)	Cd(1)-N(2)	2.342(3)
Cd(1)-O(4A)	2.323(2)	Cd(1)-O(5A)	2.566(2)
Cd(1)-O(5B)	2.312(2)	O(1)-Cd(1)-O(2)	53.12(9)
O(1)-Cd(1)-N(1)	144.28(9)	O(1)-Cd(1)-N(2)	84.42(9)
O(1)-Cd(1)-O(4A)	110.62(9)	O(1)-Cd(1)-O(5A)	81.32(8)
O(1)-Cd(1)-O(5B)	103.23(9)	O(4A)-Cd(1)-O(2)	86.82(9)
O(4A)-Cd(1)-O(5A)	52.62(8)	O(4A)-Cd(1)-N(1)	85.81(8)
O(4A)-Cd(1)-N(2)	153.82(9)	O(5B)-Cd(1)-O(2)	155.96(8)
O(5A)-Cd(1)-O(2)	103.05(7)	O(5B)-Cd(1)-O(4A)	108.31(9)
O(5B)-Cd(1)-O(5A)	74.00(8)	O(5B)-Cd(1)-N(1)	100.95(9)
N(1)-Cd(1)-O(5A)	130.94(8)	N(1)-Cd(1)-N(2)	70.61(9)
N(2)-Cd(1)-O(2)	85.69(8)	N(2)-Cd(1)-O(5A)	153.52(9)
O(5B)-Cd(1)-N(2)	87.80(8)	N(1)-Cd(1)-O(2)	98.65(9)

Symmetry transformations used to generate equivalent atoms: A: x+1, +y, 1+z**.** B: 1-x,1-y, 1-z.

Table S3. Comparison of detection capacities of **Cd-CP2** toward UA with other probes.

Luminescent material	Detection mechanism	K_{sv}/M^{-1}	Detection limit	Ref.
Cu^{2+}@MIL-91(Al : Eu)	Turn-on	----	1.6 μM	36
ZJU-158-Tb	On-off-on	8.37×10^3	7 nM	37
Eu-BDC@FM	On-off-on	1.06×10^4	0.6 μM	38
MBP-SO_3@Nafion	----	----	11.3 μM	39
Hf-UiO-66-Py	ratiometric	----	1.4 μM	40
PCN-222 (Fe)	Turn-on	----	3.5 μM	41
MOF-235	----	----	3.46 μM	42
BTB-MOF	Turn-off	----	4×10^{-4}mg/L	43
URICASE and HRP@HP-DUT-5	Turn-on	----	0.8 μM	44
CD-MONT-2	Turn-on	----	4.3 μM	45
Eu-TDA	Turn-off	4.15×10^4	0.689 μM	46
Cd-CP2	Turn-off	5.162×10^4	0.67 μM	This work

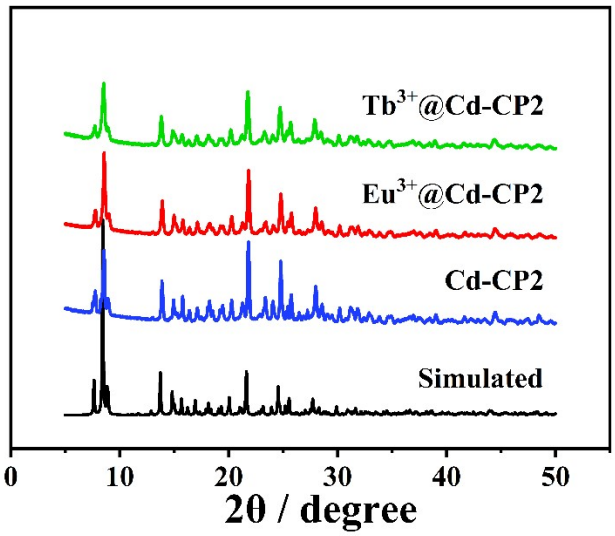

Fig. S1. PXRD of as-synthesized **Cd-CP2**, **Eu^{3+}@Cd-CP2** and **Tb^{3+}@Cd-CP2**.

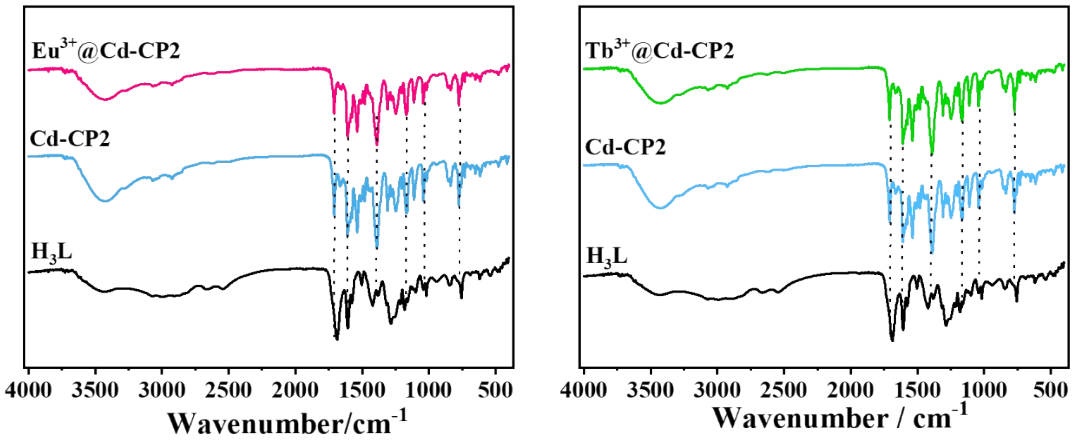

(a) **(b)**

Fig. S2. (a) FT-IR spectra of the H_3L**, Cd-CP2** and **Eu^{3+}@Cd-CP2**. (b) FT-IR spectra of H_3L, **Cd-CP2** and **Tb^{3+}@Cd-CP2**.

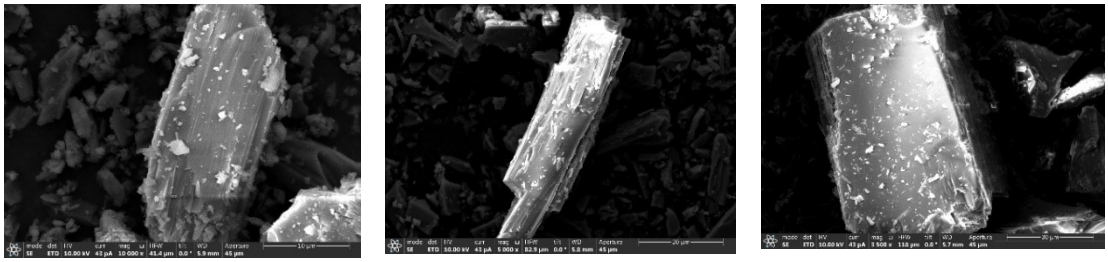

(a) (b) (c)

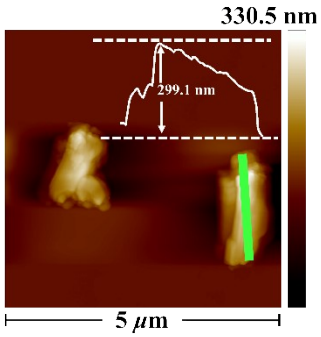

(d) (e) (f)

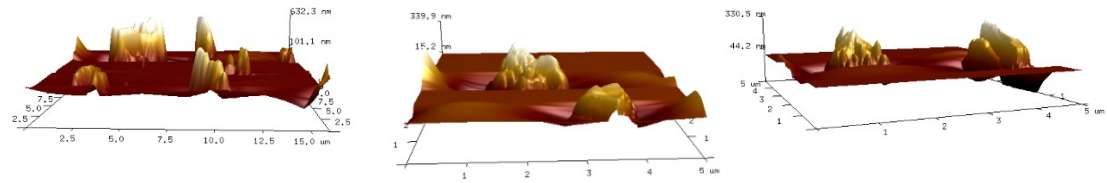

(g) (h) (i)

Fig. S3. (a-c) SEM of **Cd-CP2**, **Eu^{3+}@Cd-CP2** and **Tb^{3+}@Cd-CP2**. (d-f) 2D AFM image of **Cd-CP2**, **Eu^{3+}@Cd-CP2** and **Tb^{3+}@Cd-CP2**. (g-i) 3D AFM image of **Cd-CP2**, **Eu^{3+}@Cd-CP2** and **Tb^{3+}@Cd-CP2**.

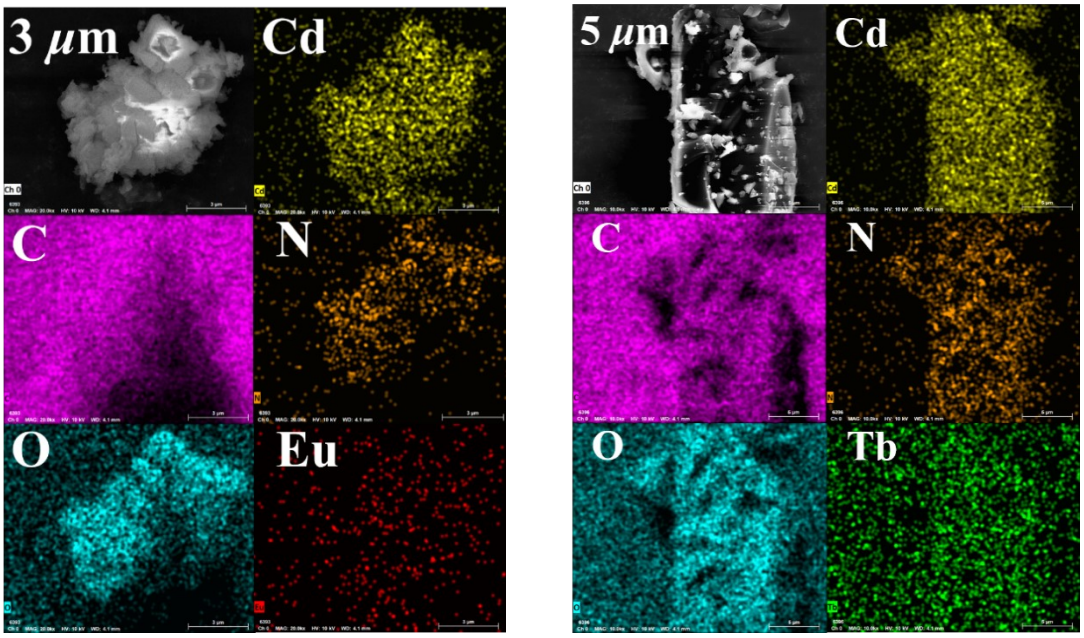

(a) **(b)**

Fig. S4. (a) EDS mapping results of **Eu^{3+}@Cd-CP2**. (b) EDS mapping results of **Tb^{3+}@Cd-CP2**.

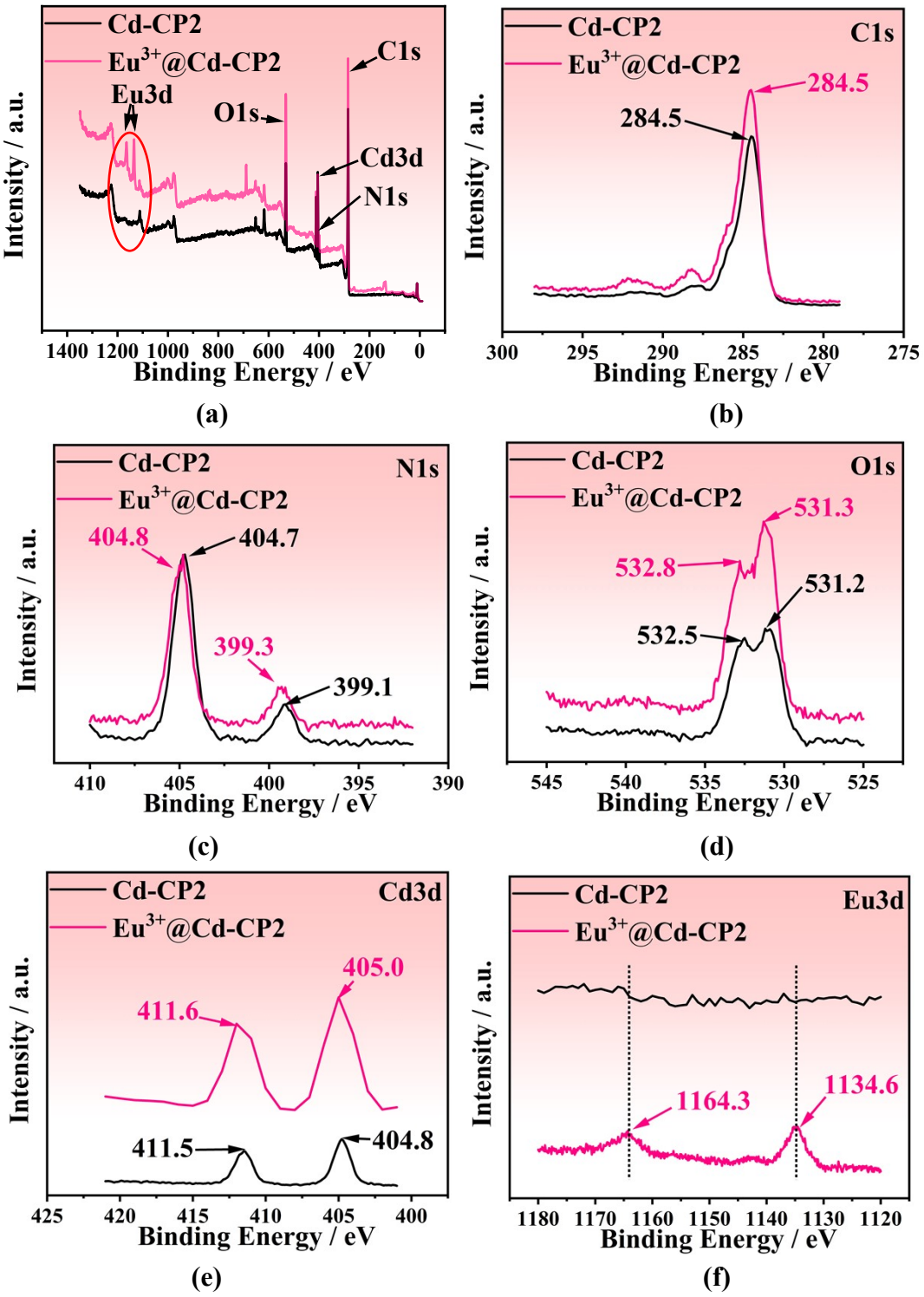

Fig. S5. (a) XPS spectra of **Cd-CP2** and **Eu^{3+}@Cd-CP2**. (b) C1s XPS, (c) N1s XPS, (d) O1s XPS, (e) Cd3d XPS, and (f) Eu3d XPS spectra of **Cd-CP2** and **Eu^{3+}@Cd-CP2**.

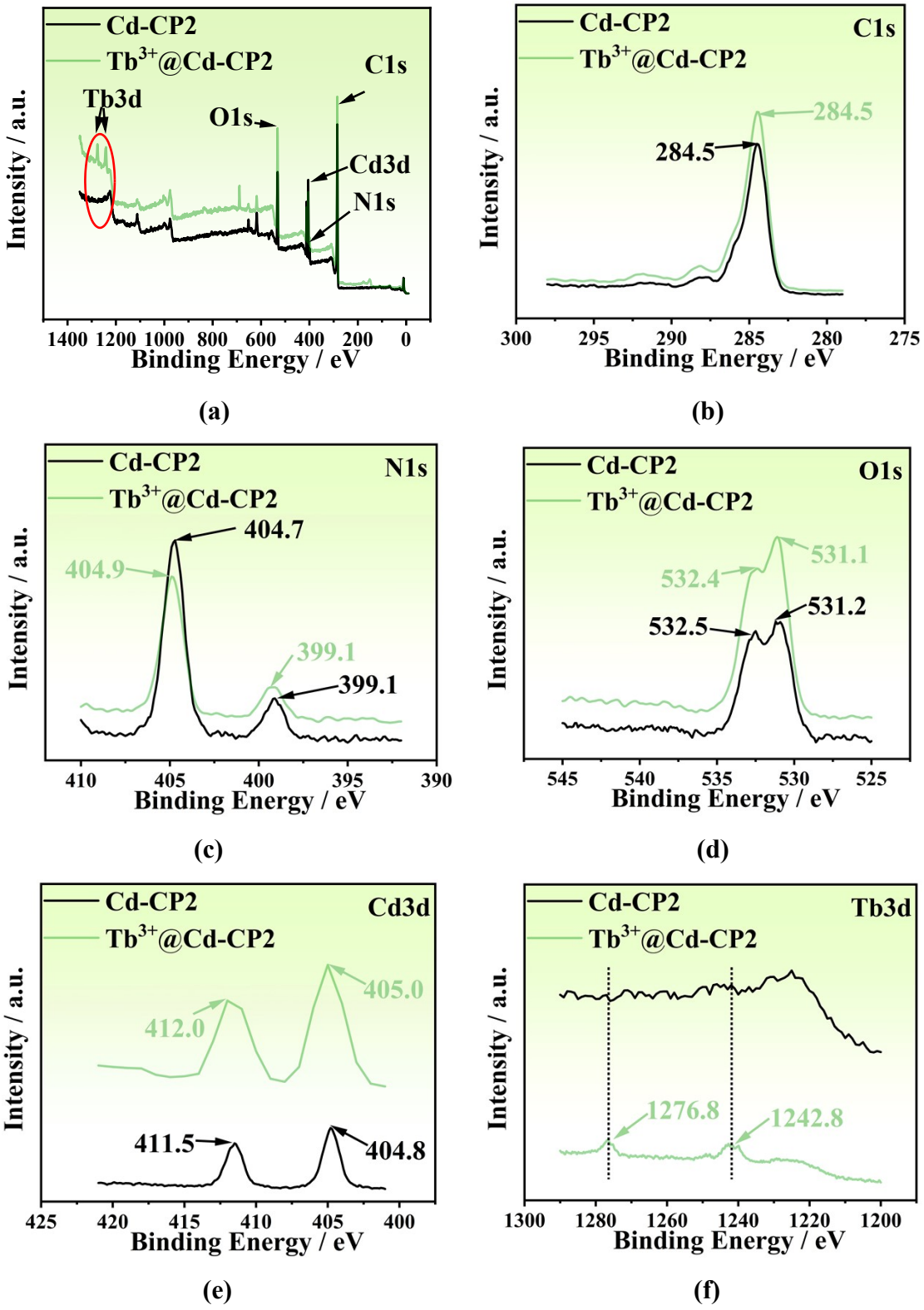

Fig. S6. (a) XPS spectra of **Cd-CP2** and **Tb^{3+}@Cd-CP2**. (b) C1s XPS, (c) N1s XPS, (d) O1s XPS, (e) Cd3d XPS, and (f) Tb3d XPS spectra of **Cd-CP2** and **Tb^{3+}@Cd-CP2**.

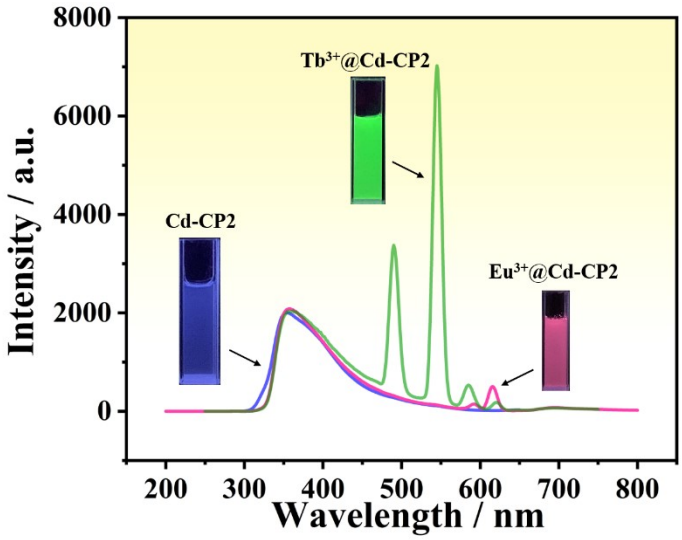

Fig. S7. Luminescence spectra and photos of aqueous suspensions of **Cd-CP2**, **Eu^{3+}@Cd-CP2**, **Tb^{3+}@Cd-CP2** under 254 nm UV light.

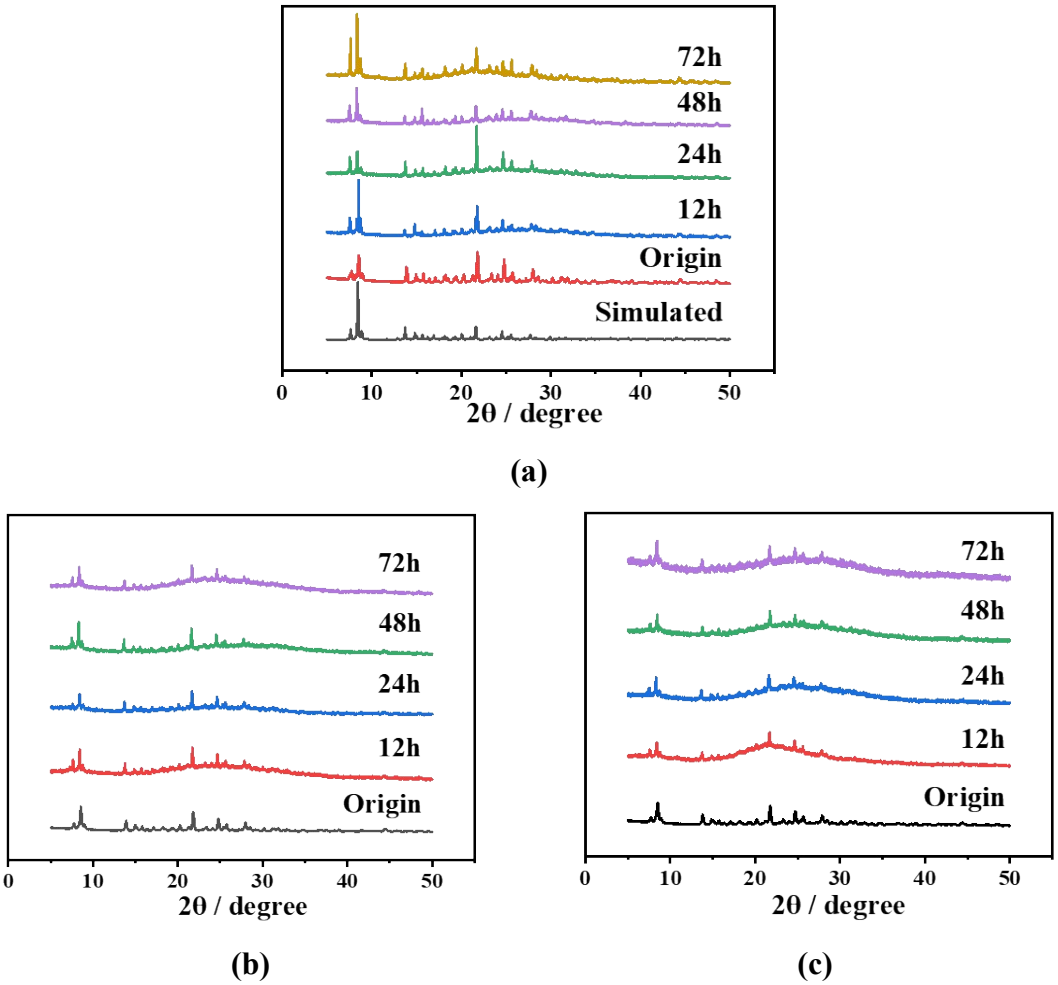

Fig. S8. (a-c) PXRD of **Cd-CP2**, **Eu^{3+}@Cd-CP2** and **Tb^{3+}@Cd-CP2** after being immersed in H_2O for different time.

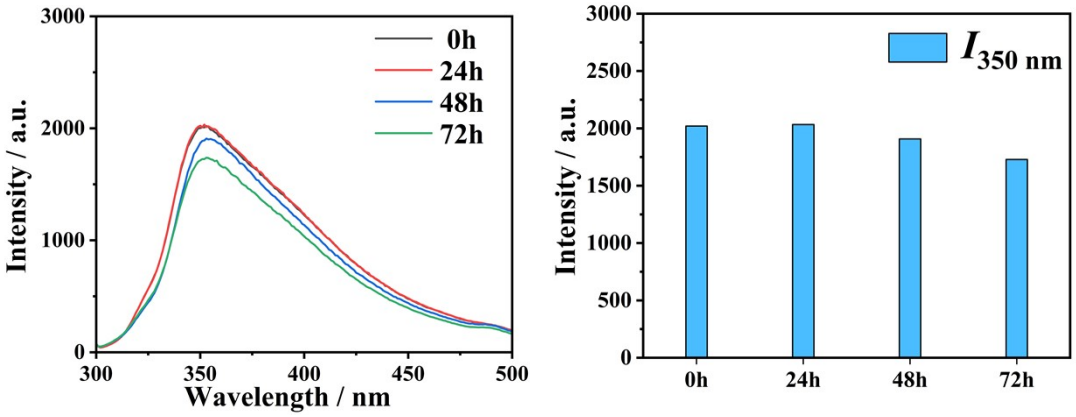

Fig. S9. (a) Emission spectra of **Cd-CP2** after being immersed in H_2O for different time; (b) The corresponding intensity histogram diagram of $I_{350\ nm}$.

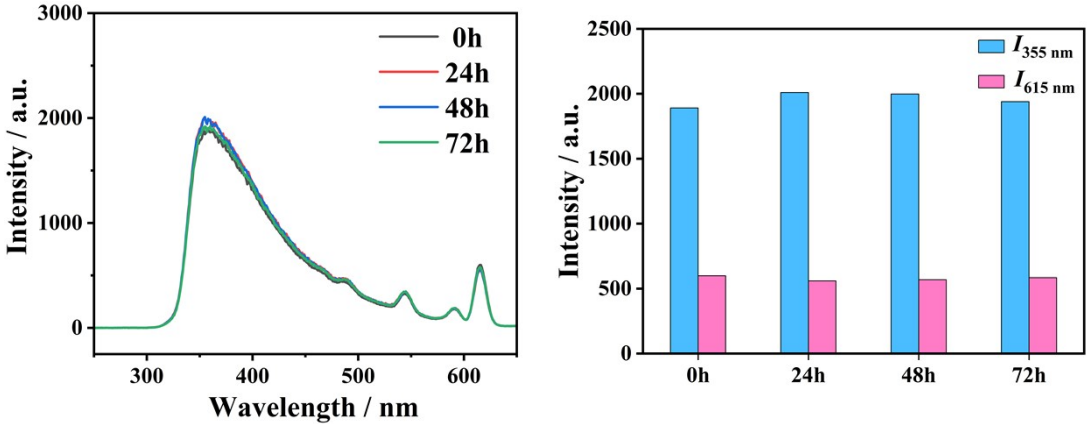

Fig. S10. (a) Emission spectra of **Eu^{3+}@Cd-CP2** after being immersed in H_2O for different time; (b) The corresponding intensity histogram diagram of $I_{355\ nm}$ and $I_{615\ nm}$.

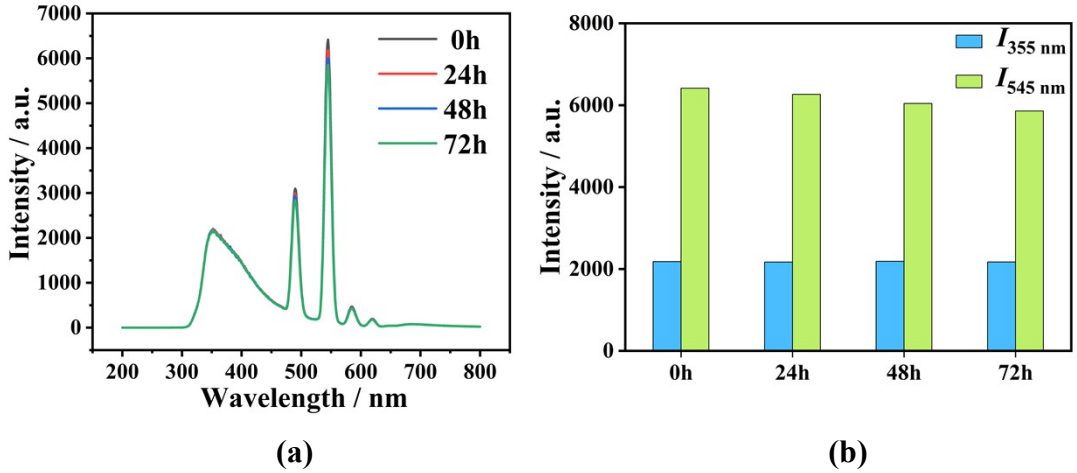

Fig. S11. (a) Emission spectra of **Tb^{3+}@Cd-CP2** after being immersed in H_2O for different time; (b) The corresponding intensity histogram diagram of $I_{355\ nm}$ and $I_{545\ nm}$.

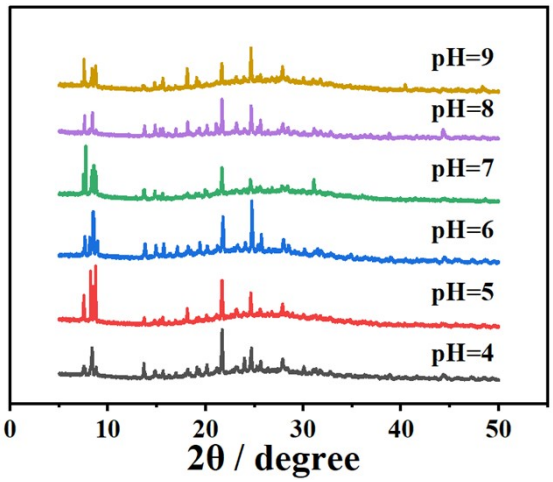

(a)

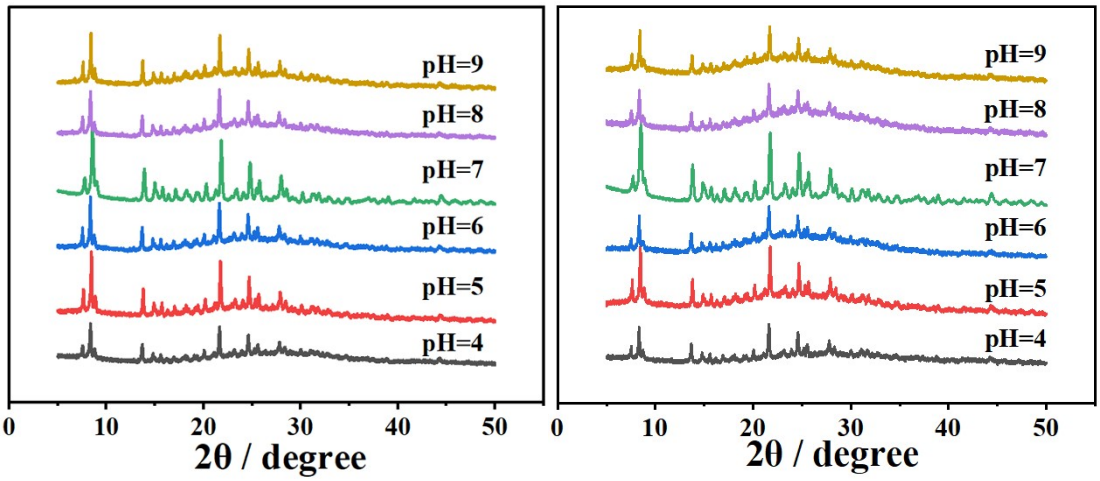

(b) **(c)**

Fig. S12. (a-c) PXRD of **Cd-CP2**, **Eu^{3+}@Cd-CP2** and **Tb^{3+}@Cd-CP2** after being immersed in the solutions of pH = 4-9.

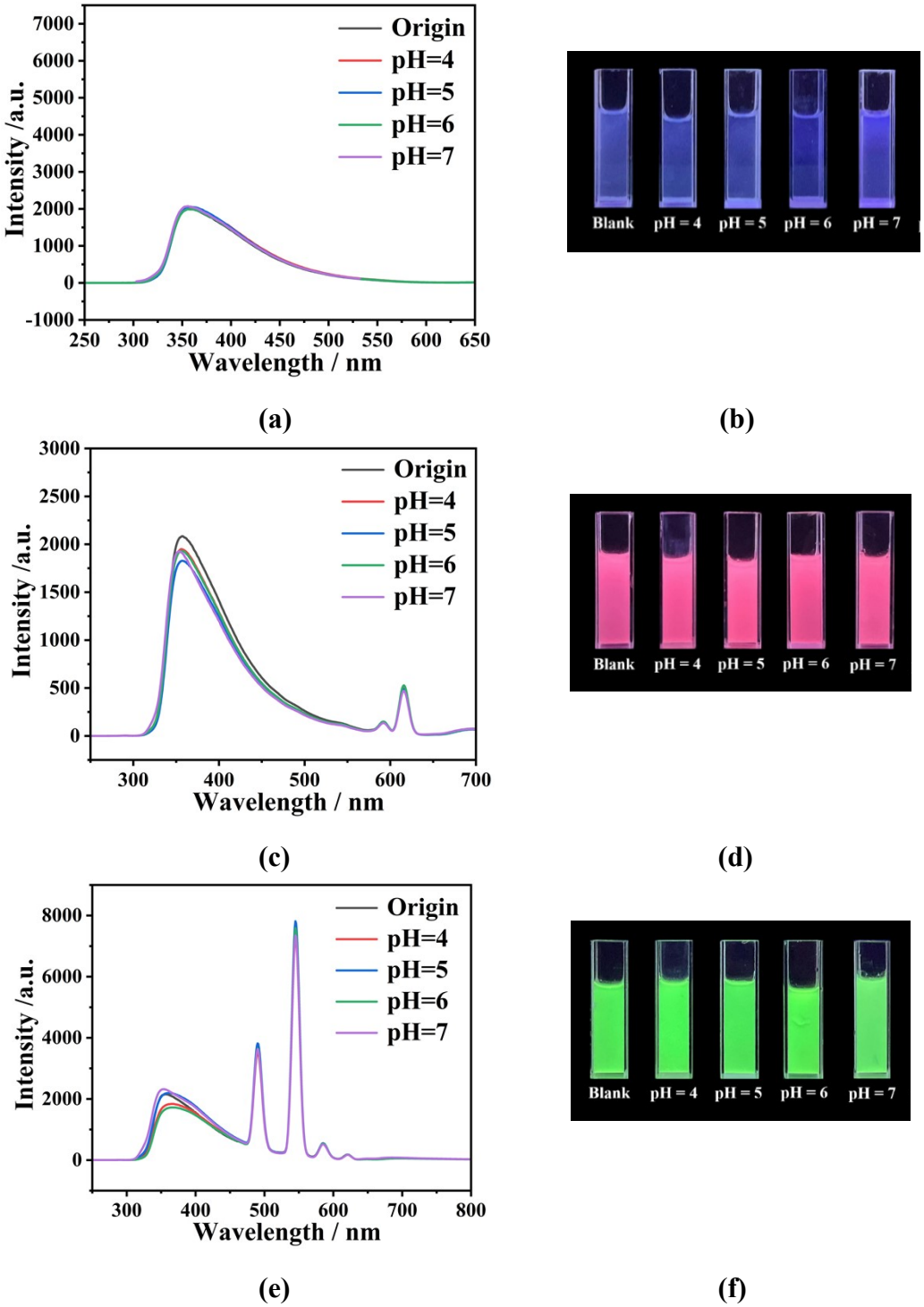

Fig. S13. (a) The emission spectra of **Cd-CP2** after immersing in aqueous solutions with different pH values. (b) The photo of **Cd-CP2** in different pH values irradiated by 254 nm UV lamp. (c) The emission spectra of **Eu^{3+}@Cd-CP2** after immersing in aqueous solutions with different pH values. (d) The photo of **Eu^{3+}@Cd-CP2** in different pH values irradiated by 254 nm UV lamp. (e) The emission spectra of **Tb^{3+}@Cd-CP2** after immersing in aqueous solutions with different pH values. (f) The photo of **Tb^{3+}@Cd-CP2** in different pH values irradiated by 254 nm UV lamp.

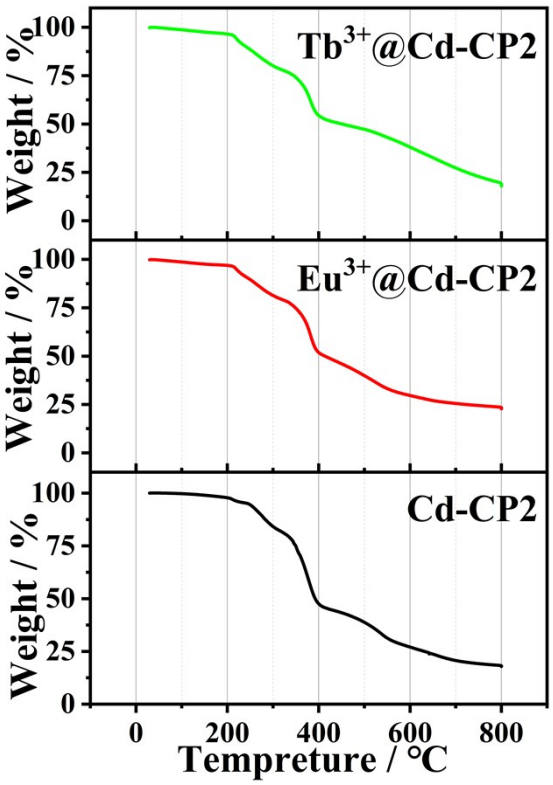

Fig. S14. TG of **Cd-CP2, Eu^{3+}@Cd-CP2, Tb^{3+}@Cd-CP2**.

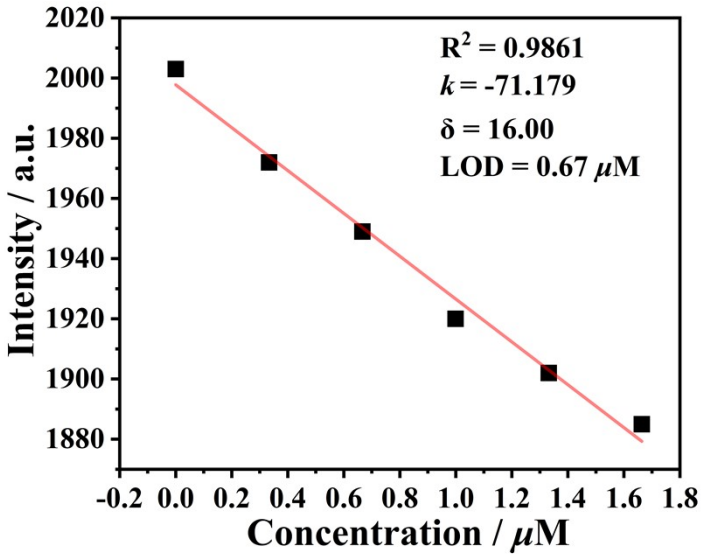

Fig. S15. The detection limit calculation of **Cd-CP2 (**10^{-3} M**)** towards UA based on the intensity of 350 nm.

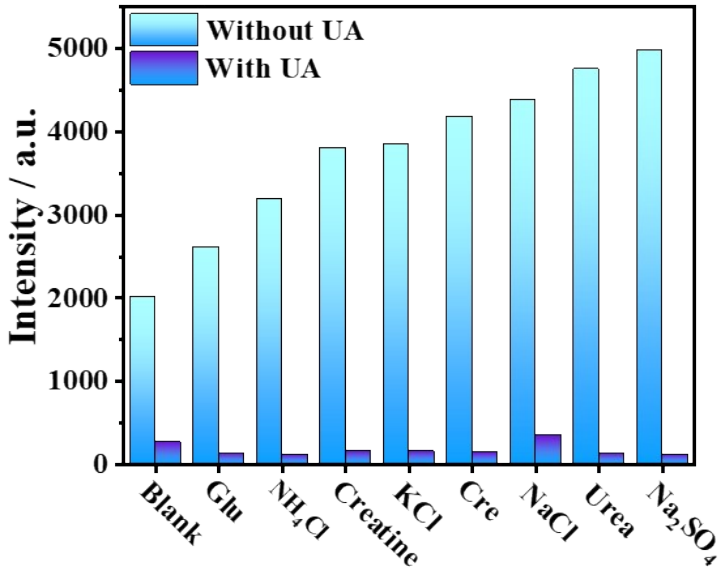

Fig. S16. Luminescence intensities of **Cd-CP2** toward other urine components with and without UA based on the intensity at 350 nm.

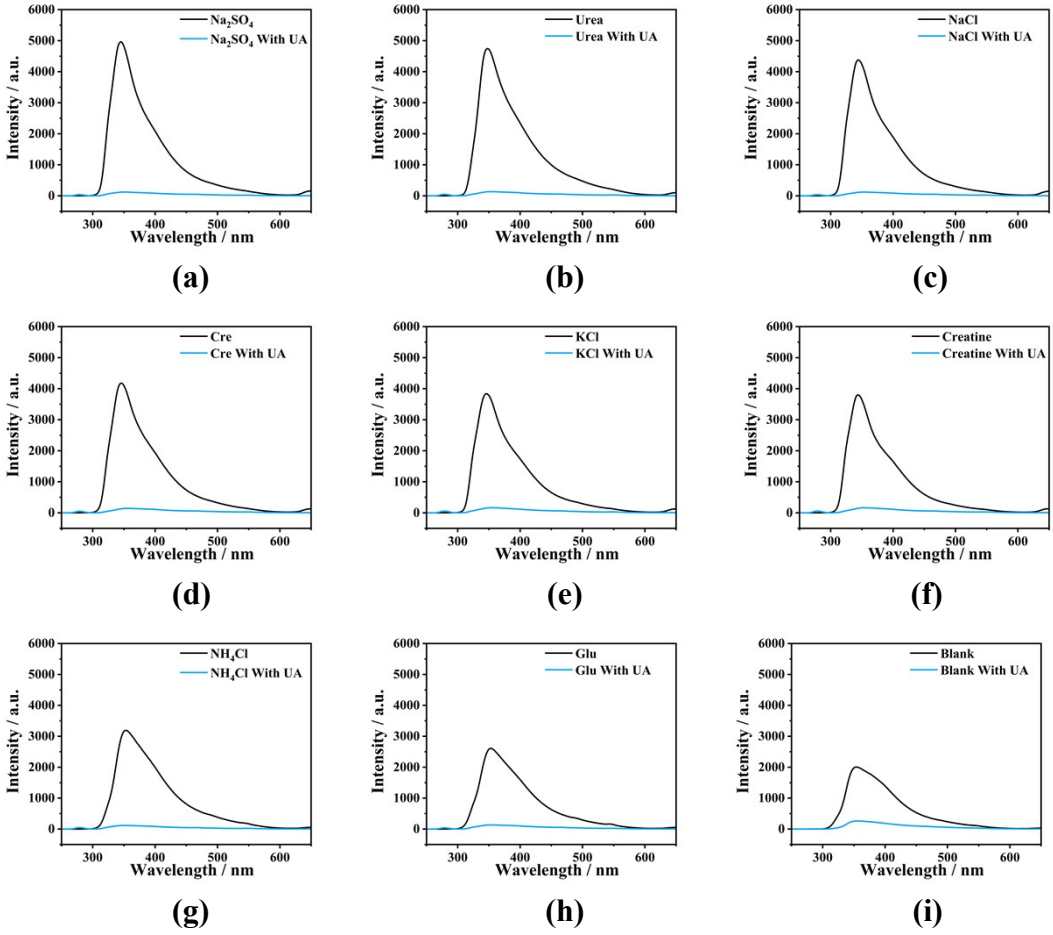

Fig. S17. (a-i) The luminescence emission of **Cd-CP2** toward other urine components with and without UA.

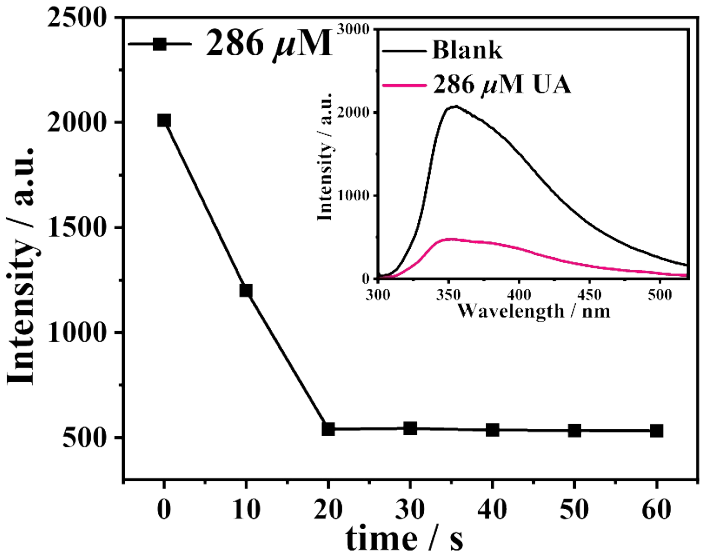

Fig. S18. Response time of **Cd-CP2** toward UA based on the intensity at 350 nm.

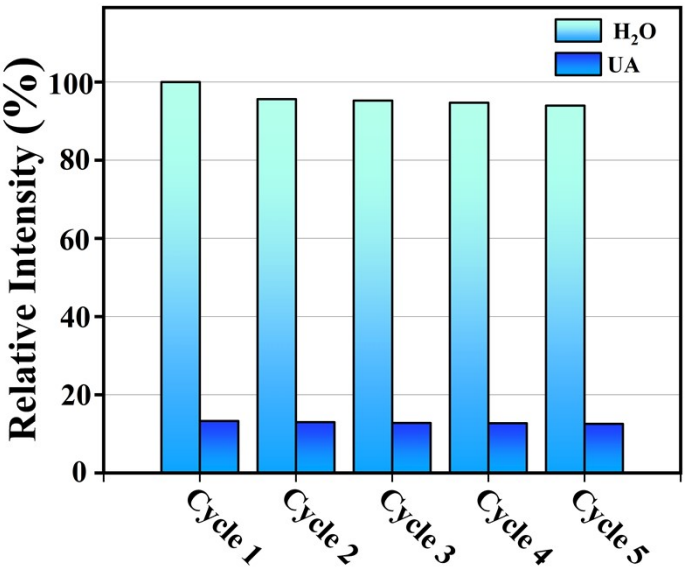

Fig. S19. The repeatability of **Cd-CP2** in sensing of UA based on the intensity at 350 nm within five cycles.

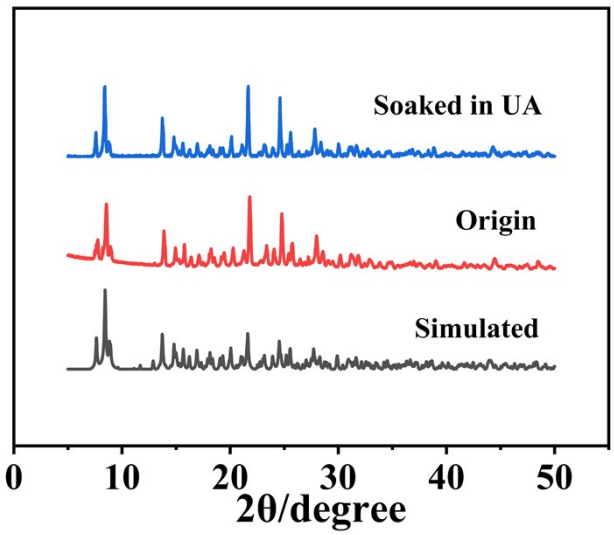

Fig. S20. PXRD of **Cd-CP2** after being immersed in UA solutions (10^{-3} M).

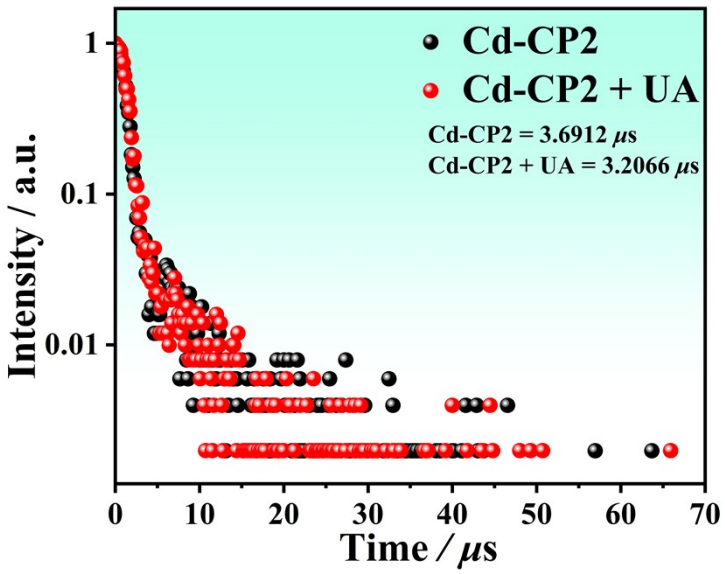

Fig. S21. The luminescence lifetime decay curves of **Cd-CP2** and **Cd-CP2** with UA.

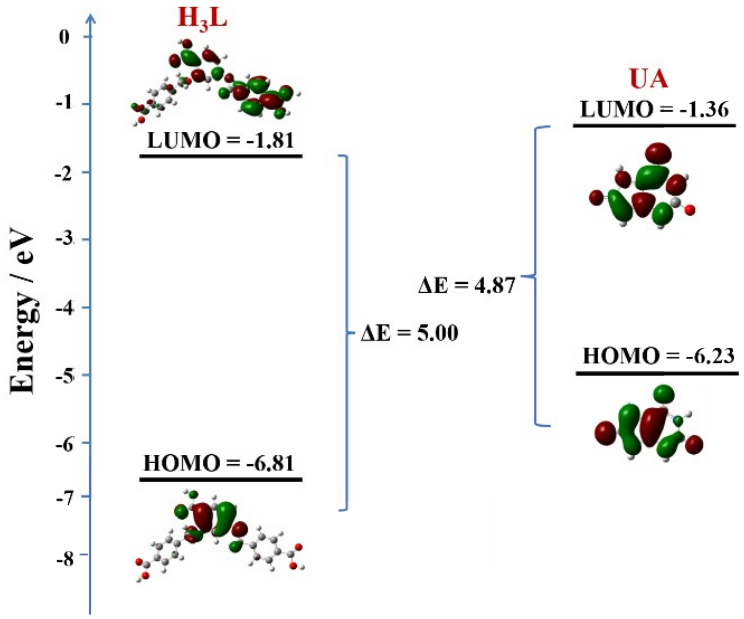

Fig. S22. The calculated HOMO and LUMO energy levels of H_3L and UA.

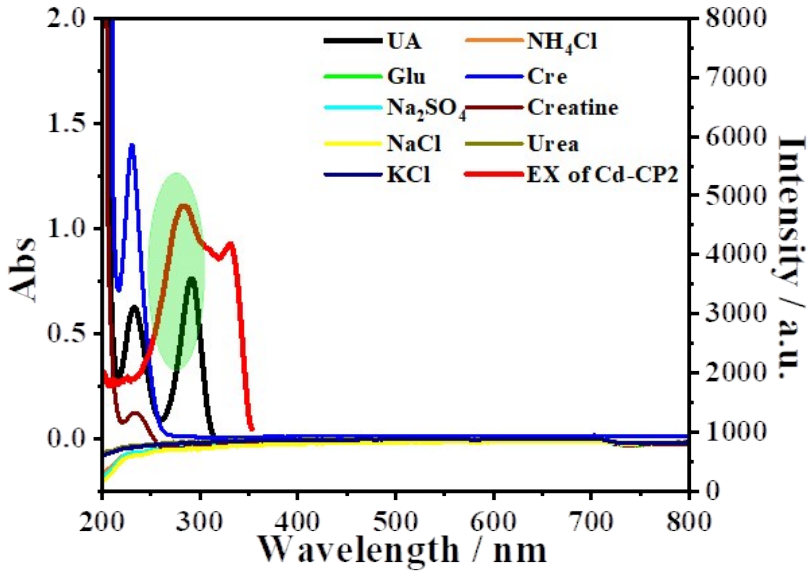

Fig. S23. UV−vis absorption spectra of various urine chemicals and excitation of **Cd-CP2**.

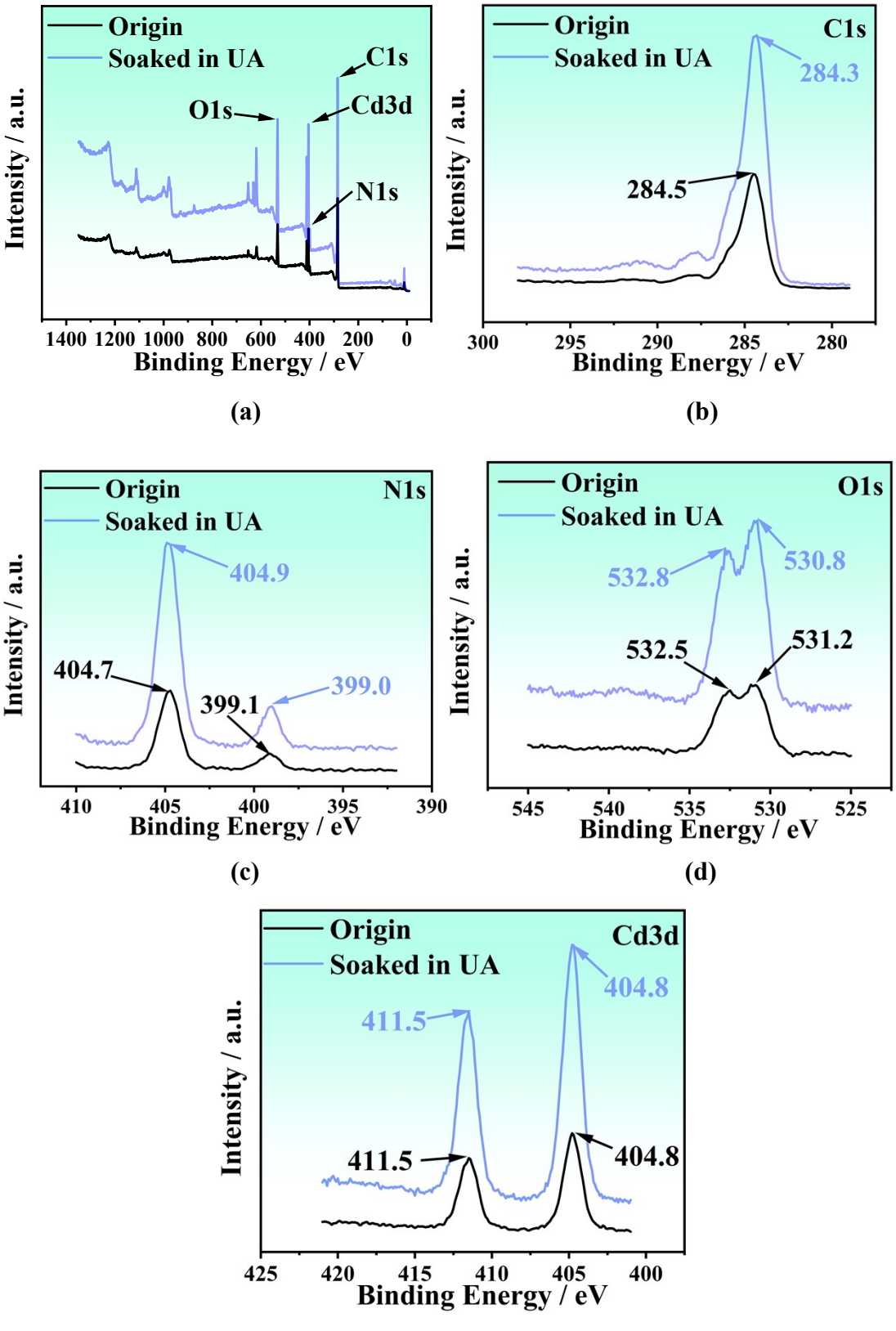

Fig. S24. (a) XPS of **Cd-CP2** before and after immersing in 10^{-3} M UA aqueous solutions. (b) C1s XPS, (c) N1s XPS, (d) O1s XPS and (e) Cd3d XPS of **Cd-CP2** before and after immersing in 10^{-3} M UA aqueous solutions.

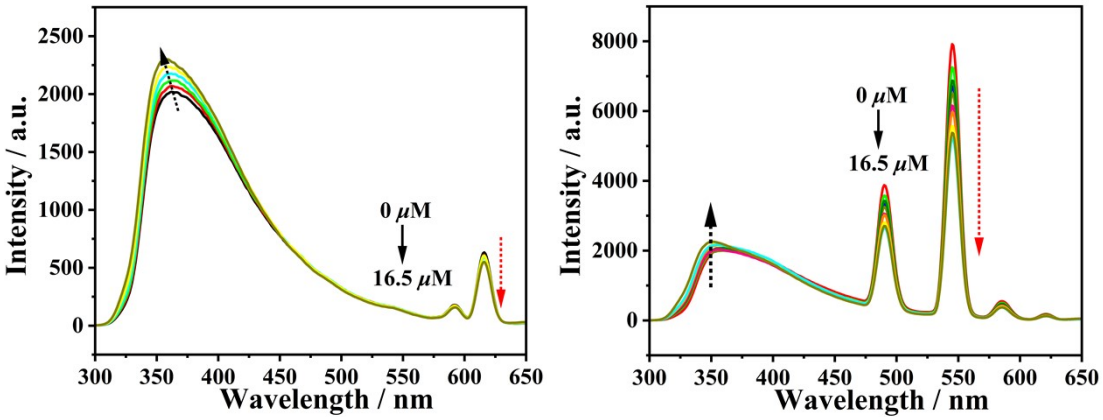

Fig. S25. (a) Luminescence titration of **Eu^{3+}@Cd-CP2** toward UA in the low concentration range. (b) Luminescence titration of **Tb^{3+}@Cd-CP2** toward UA in the low concentration range.

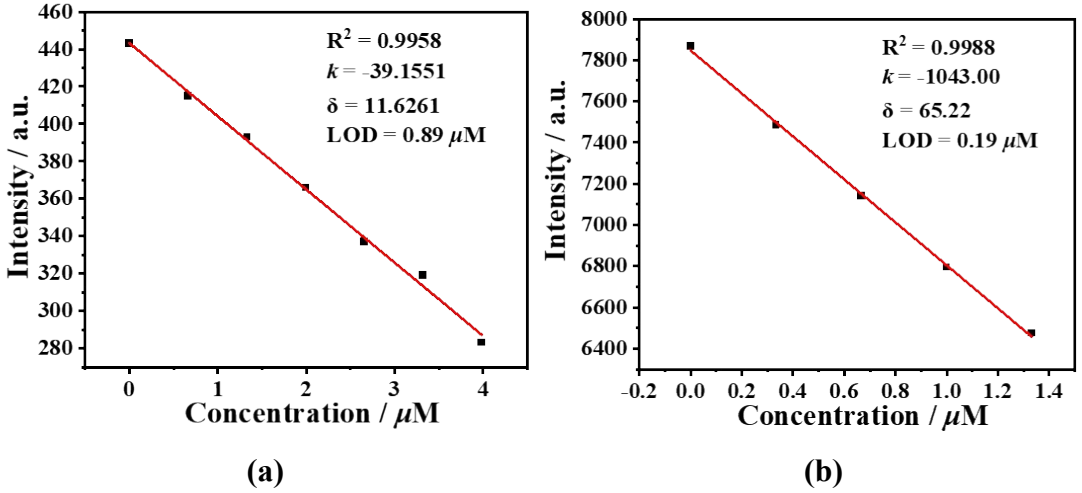

(a) **(b)**

Fig. S26. (a) The detection limit calculation of **Eu^{3+}@Cd-CP2** towards NANA based on the intensity at 615 nm. (b) The detection limit calculation of **Tb^{3+}@Cd-CP2** towards NANA based on the intensity at 545 nm.

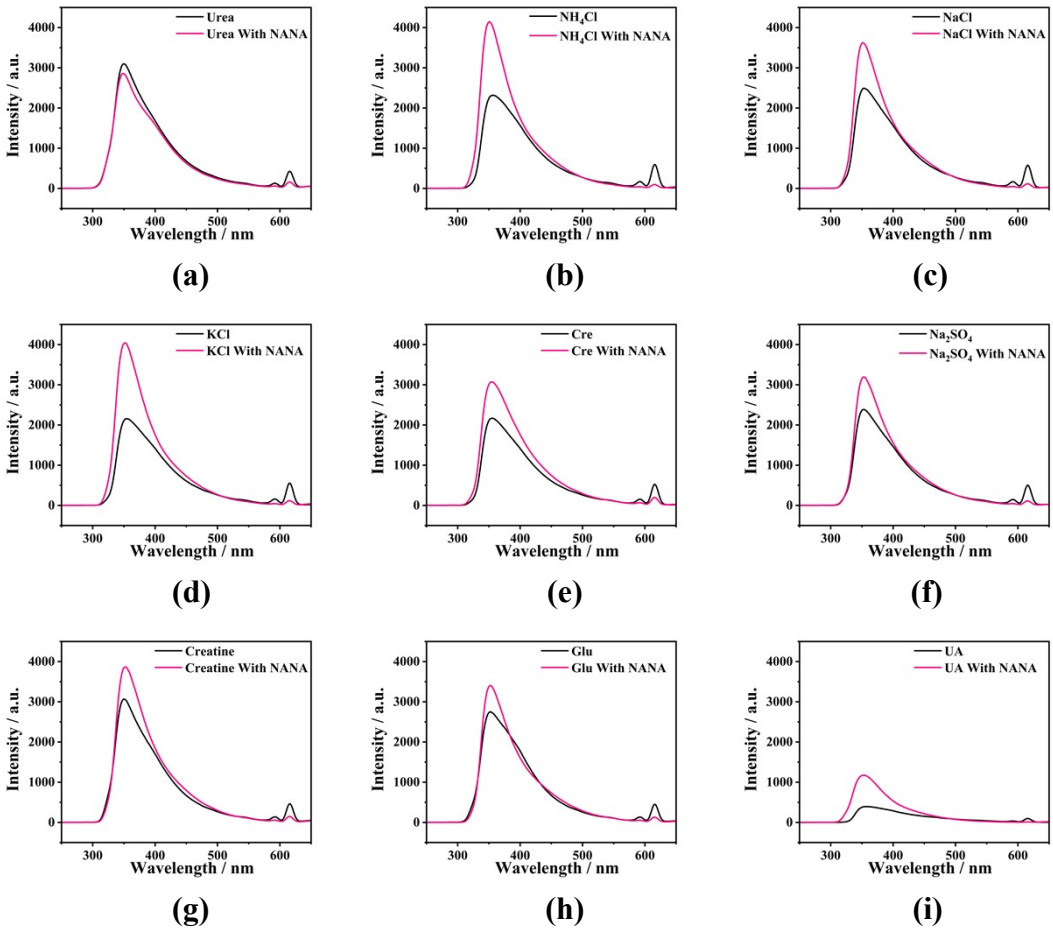

Fig. S27. (a-i) The luminescence emission of **Eu^{3+}@Cd-CP2** toward other urine components with and without NANA.

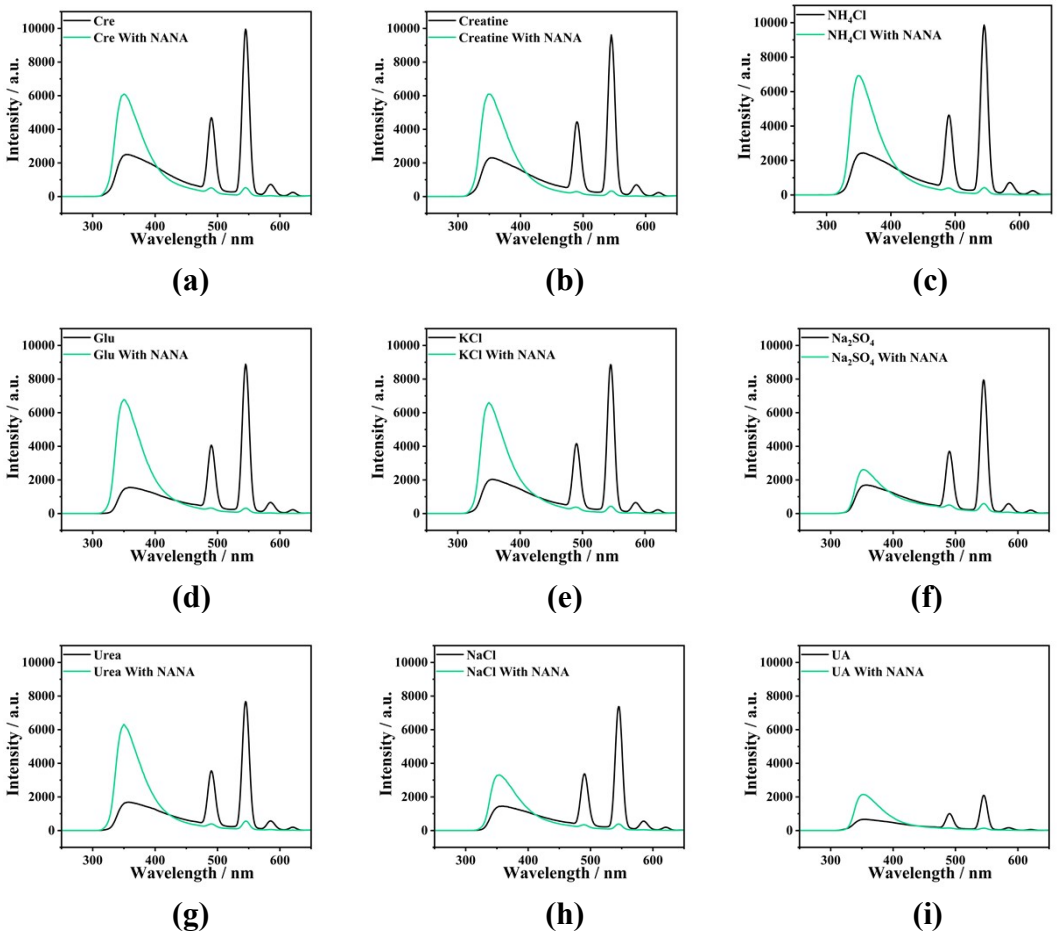

Fig. S28. (a-i) The luminescence emission of **Tb^{3+}@Cd-CP2** toward other urine components with and without NANA.

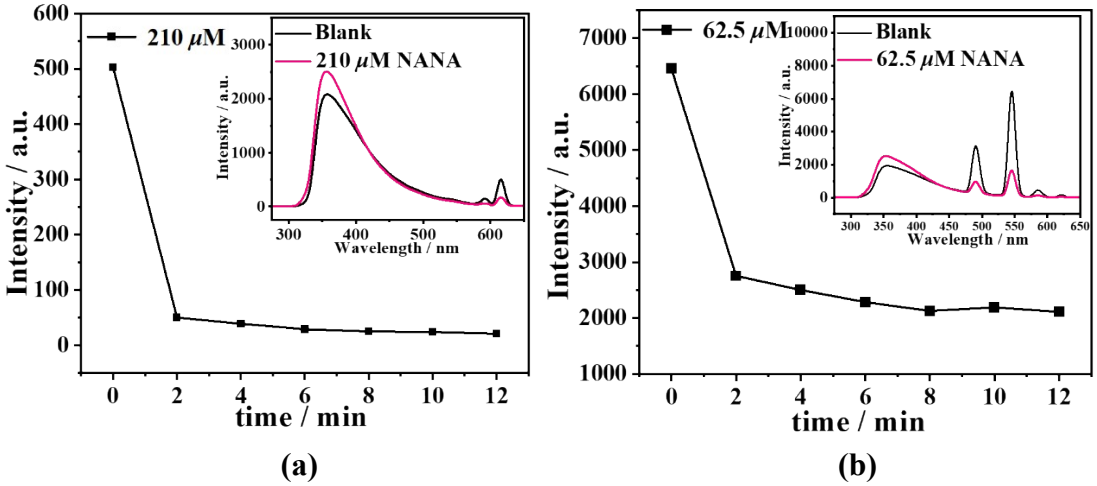

Fig. S29. (a) Response time of **Eu^{3+}@Cd-CP2** toward NANA based on the intensity at 615 nm. (b) Response time of **Tb^{3+}@Cd-CP2** toward NANA based on the intensity at 545 nm.

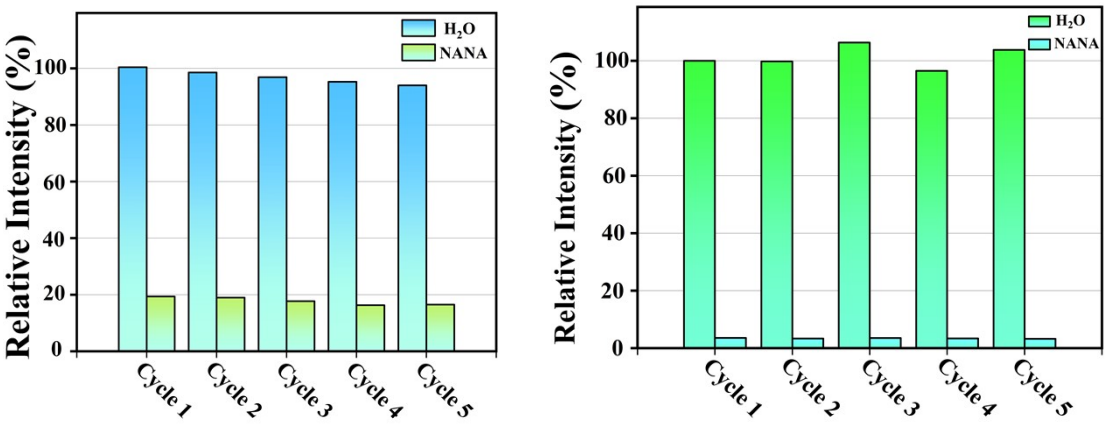

Fig. S30. (a) The repeatability of **Eu^{3+}@Cd-CP2** based on the intensity at 545 nm in sensing of NANA. (b) The repeatability of **Tb^{3+}@Cd-CP2** based on the intensity at 545 nm in sensing of NANA.

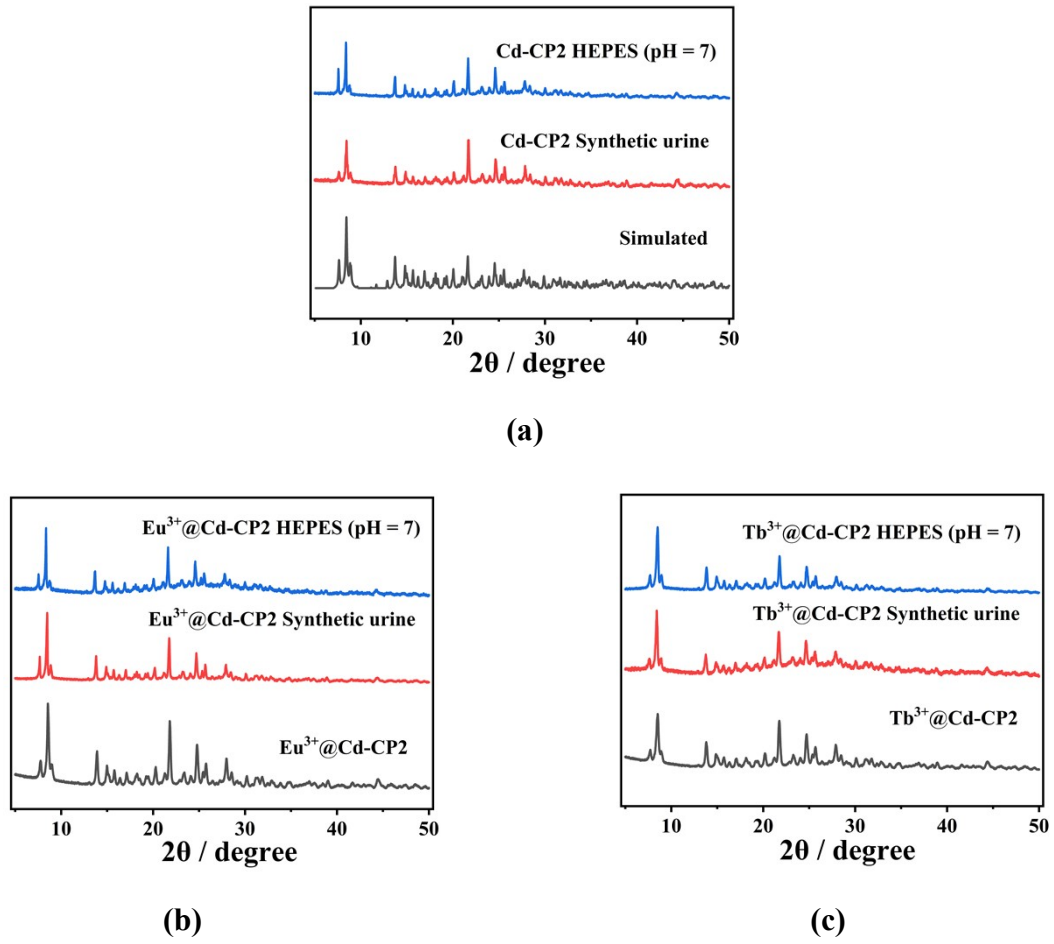

Fig. S31. (a-c) PXRD of **Cd-CP2**, **Eu^{3+}@Cd-CP2** and **Tb^{3+}@Cd-CP2** after being immersed in the solutions of synthetic urine or HEPES buffer solution (pH = 7.0).

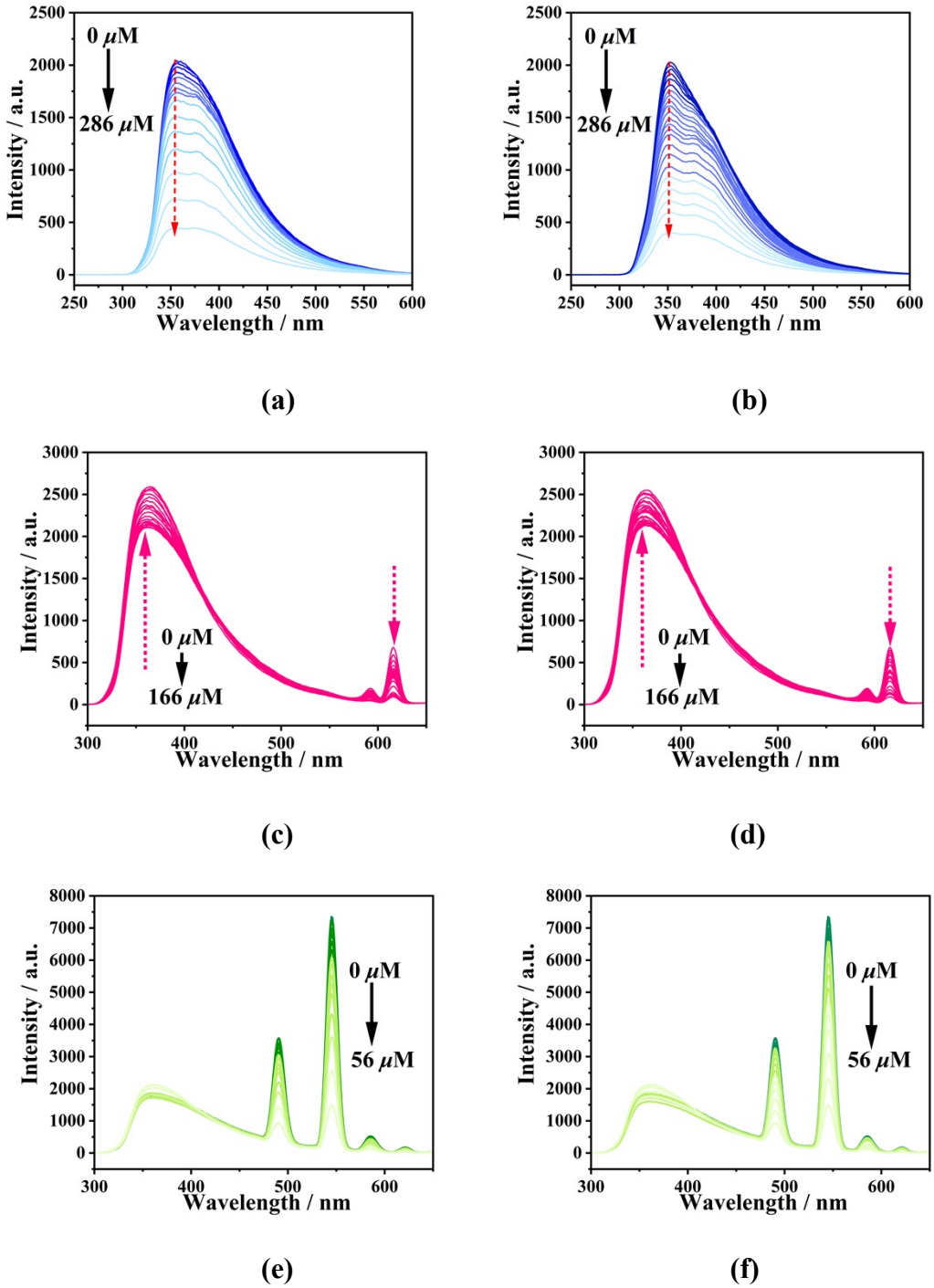

Fig. S32. (a-b) Luminescence titration result of **Cd-CP2** toward UA in synthetic urine and HEPES buffer solution (pH = 7.0). (c-d) Luminescence titration result of **Eu^{3+}@Cd-CP2** toward NANA in synthetic urine and HEPES buffer solution (pH = 7.0). (e-f) Luminescence titration result of **Tb^{3+}@Cd-CP2** toward UA in synthetic urine and HEPES buffer solution (pH = 7.0).

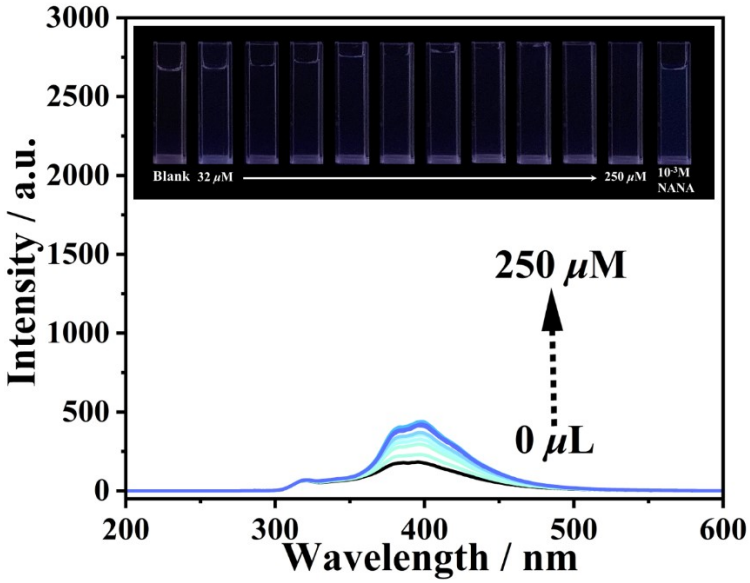

Fig. S33. Fluorescence spectra of different concentrations of NANA and photographs under 254 nm UV lamps.

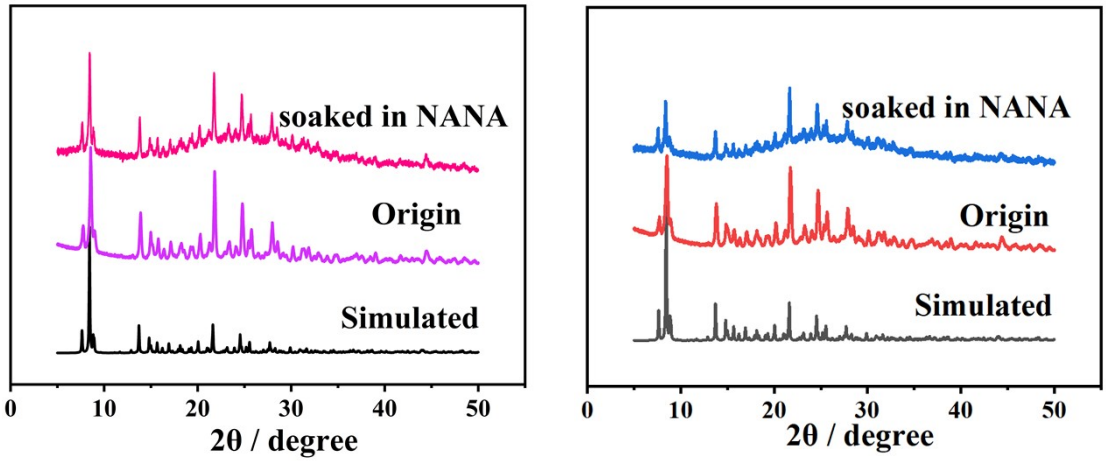

(a) **(b)**

Fig. S34. (a) PXRD of **Eu^{3+}@Cd-CP2** after being immersed in the solutions of NANA. (b) PXRD of **Tb^{3+}@Cd-CP2** after being immersed in the solutions of NANA.

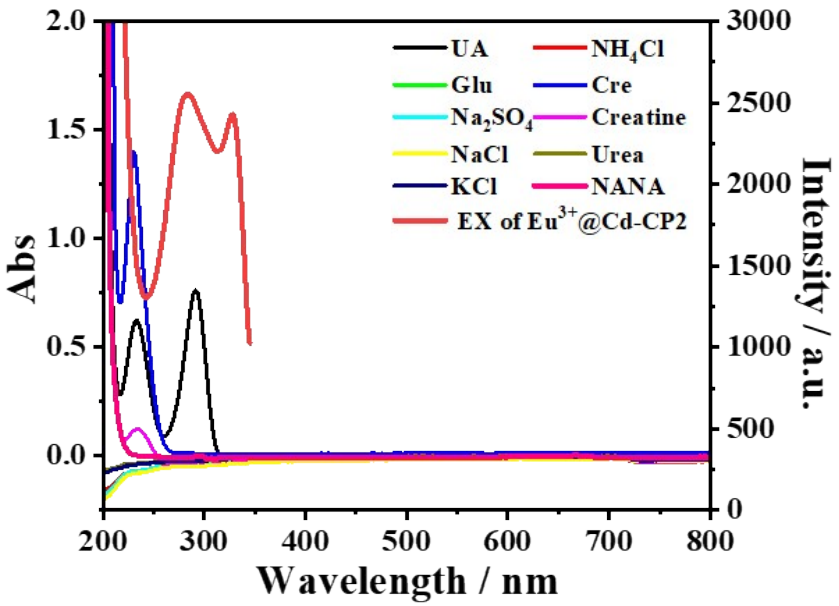

(a)

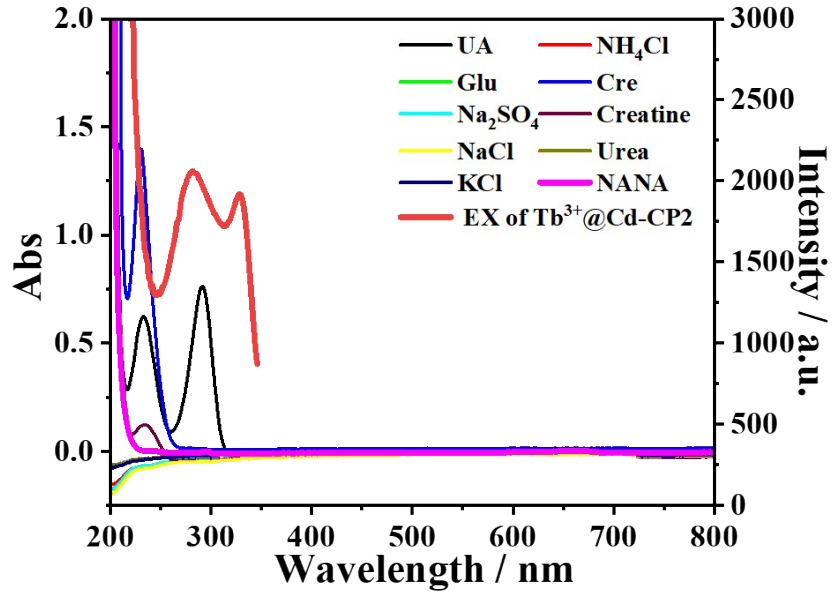

(b)

Fig. S35. (a) UV−vis absorption spectra of various urine chemicals and excitation spectra of **Eu^{3+}@Cd-CP2**. (b) UV−vis absorption spectra of various urine chemicals and excitation spectra of **Tb^{3+}@Cd-CP2**.

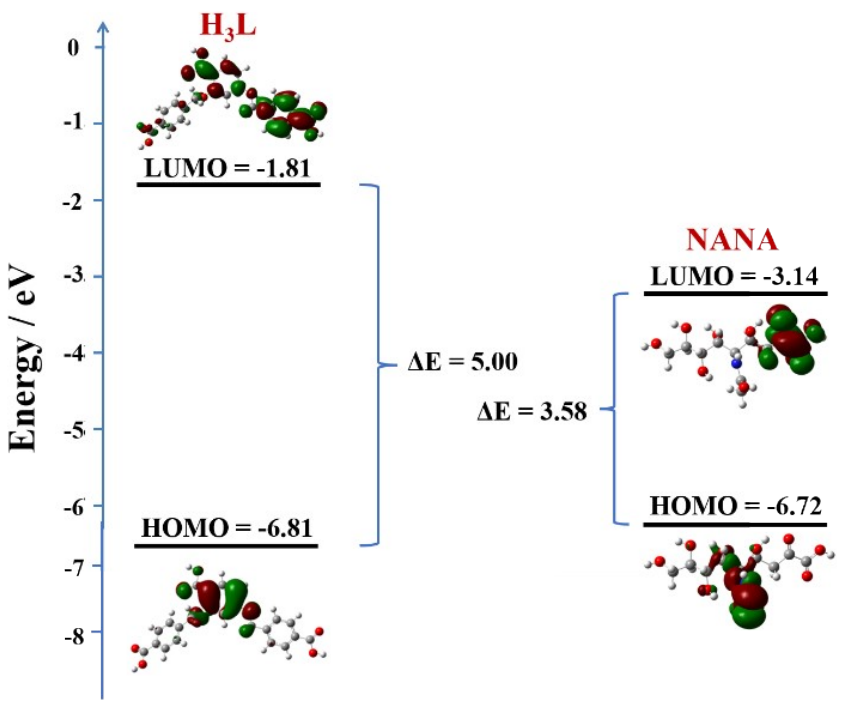

Fig. S36. The calculated HOMO and LUMO energy levels of H_3L and NANA.

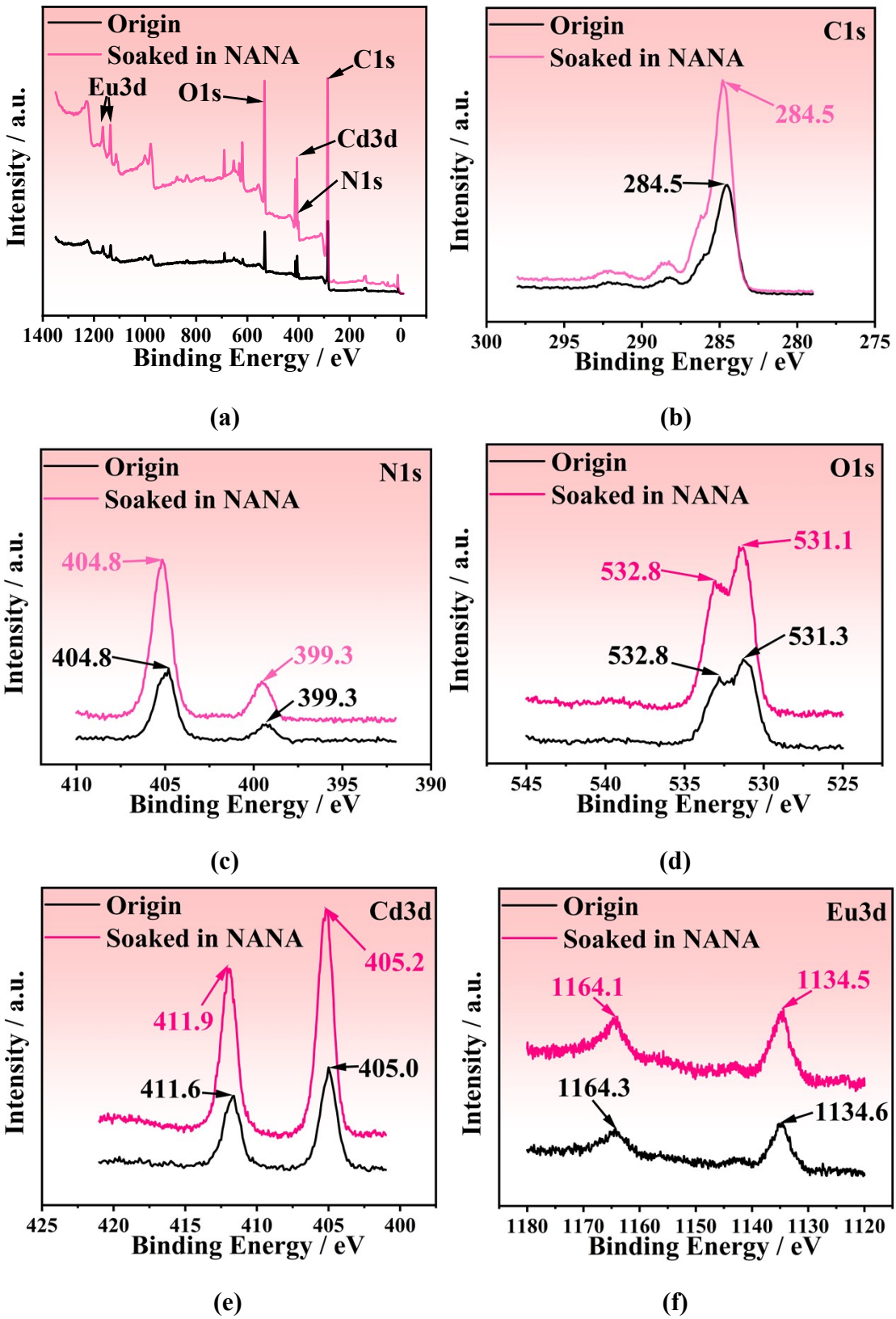

Fig. S37. (a) XPS of **Eu^{3+}@Cd-CP2** before and after immersing in 10^{-3} M NANA aqueous solutions. (b) C1s XPS, (c) N1s XPS, (d) O1s XPS, (e) Cd3d XPS, and (f) Eu3d XPS of **Eu^{3+}@Cd-CP2** before and after immersing in 10^{-3} M NANA aqueous solutions.

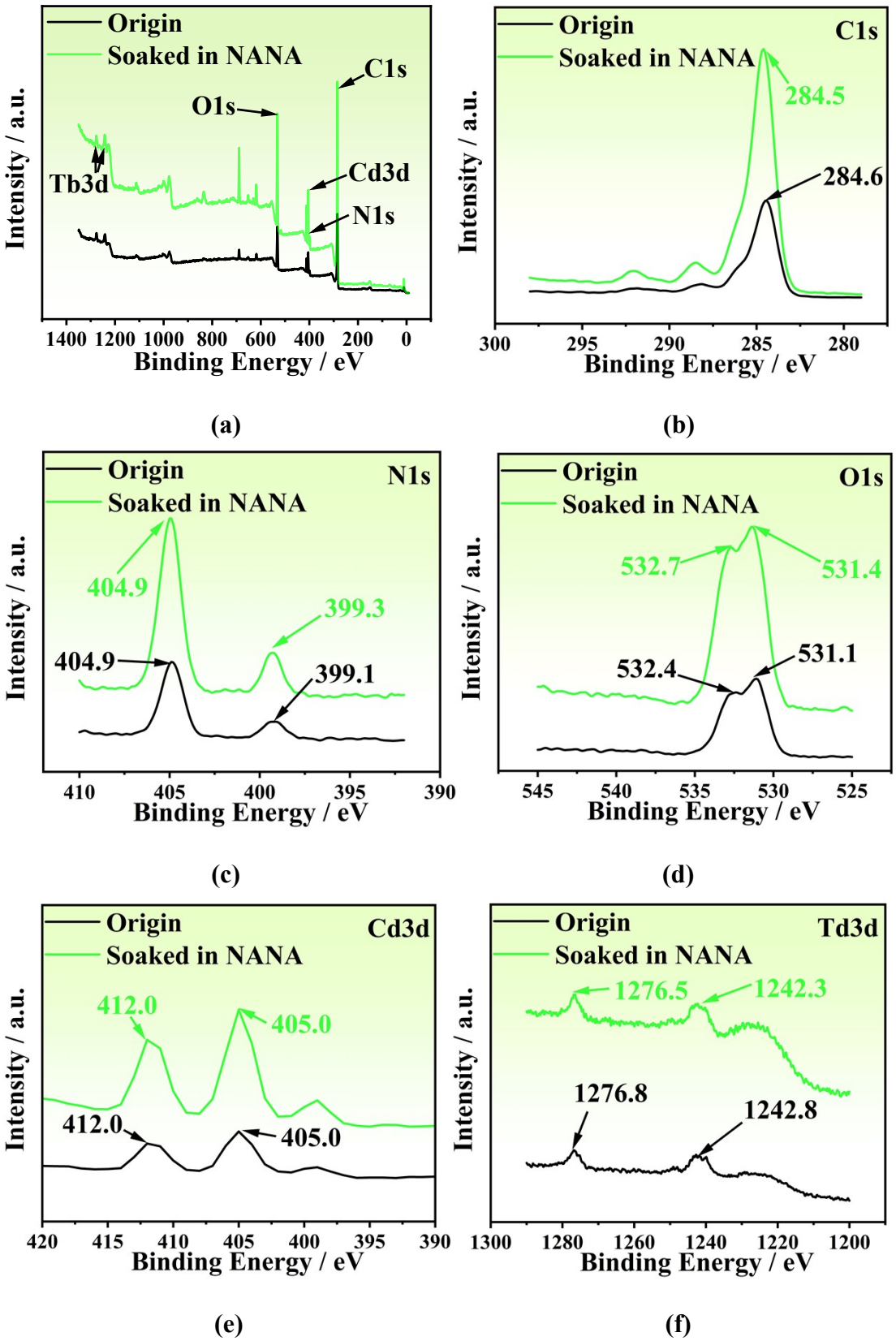

Fig. S38. (a) XPS of **Tb^{3+}@Cd-CP2** before and after immersing in 10^{-3} M NANA aqueous solutions. (b) C1s XPS, (c) N1s XPS, (d) O1s XPS, (e) Cd3d XPS, and (f) Td3d XPS of **Tb^{3+}@Cd-CP2** before and after immersing in 10^{-3} M NANA aqueous solutions.

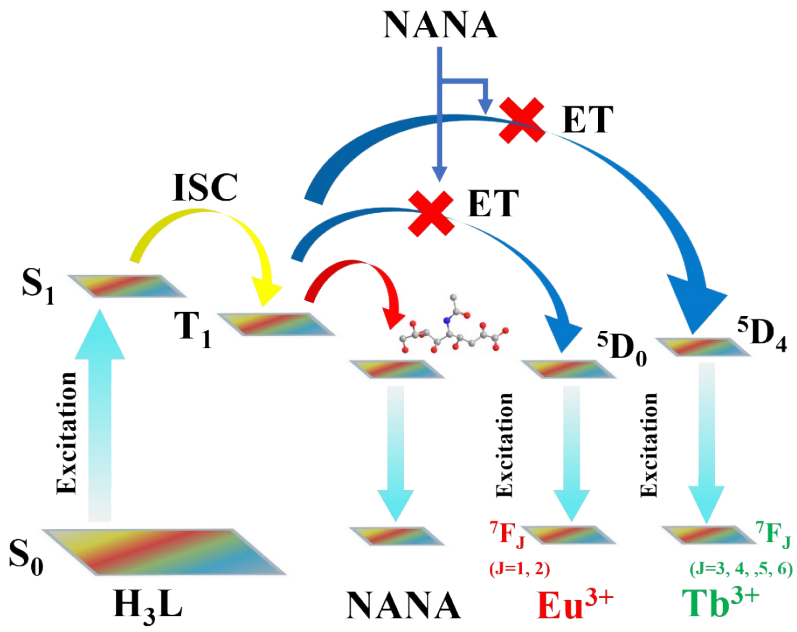

Fig. S39. Simplified schematic diagram of the energy transfer from the ligand to Eu^{3+} and Tb^{3+} ions and the mechanism of luminescence quenching.

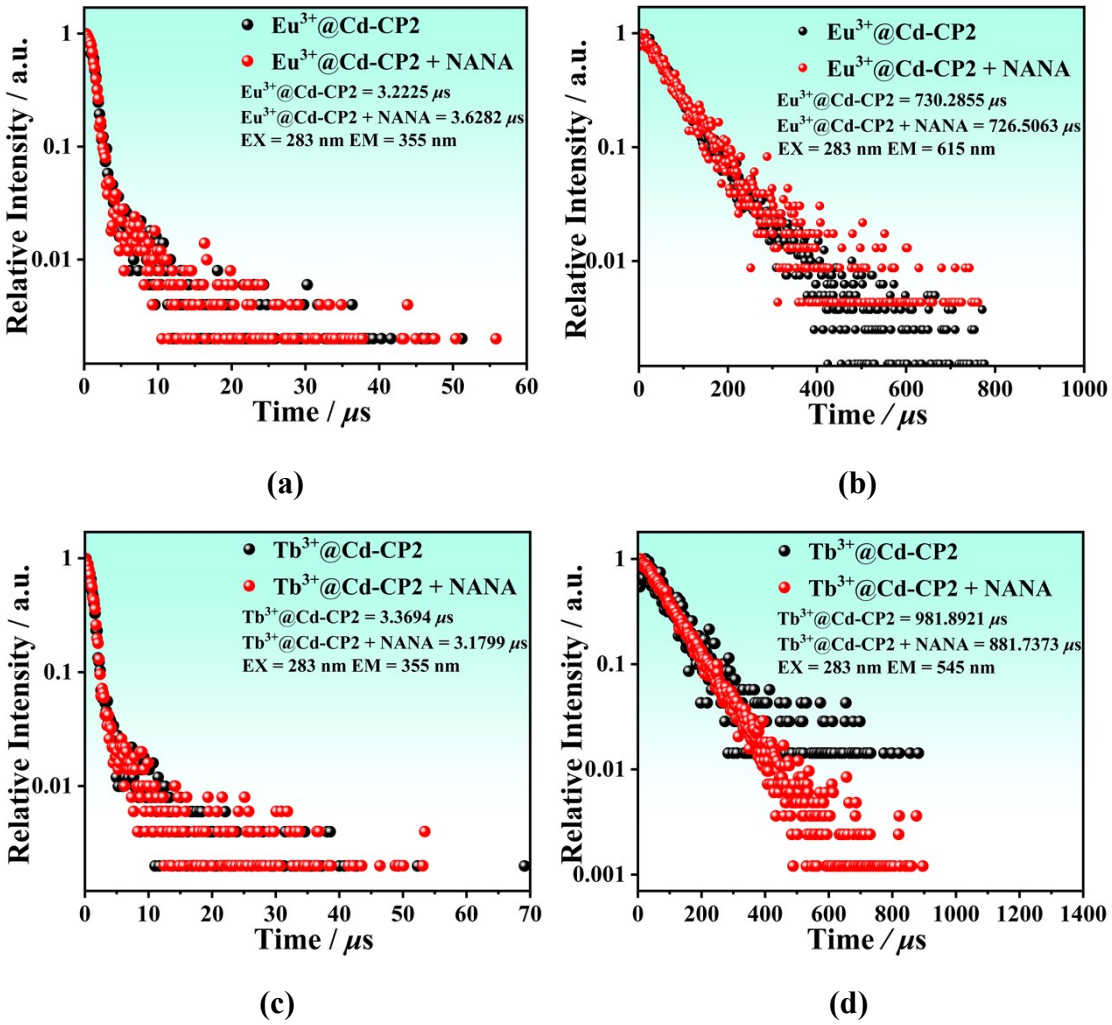

Fig. S40. (a) The luminescence lifetime decay curves of $I_{355\ nm}$ of **Eu^{3+}@Cd-CP2** and **Eu^{3+}@Cd-CP2** with NANA. (b) The luminescence lifetime decay curves of $I_{615\ nm}$ of **Eu^{3+}@Cd-CP2** and **Eu^{3+}@Cd-CP2** with NANA. (c) The luminescence lifetime decay curves of $I_{355\ nm}$ of **Tb^{3+}@Cd-CP2** and **Tb^{3+}@Cd-CP2** with NANA. (d) The luminescence lifetime decay curves of $I_{545\ nm}$ of **Tb^{3+}@Cd-CP2** and **Tb^{3+}@Cd-CP2** with NANA.

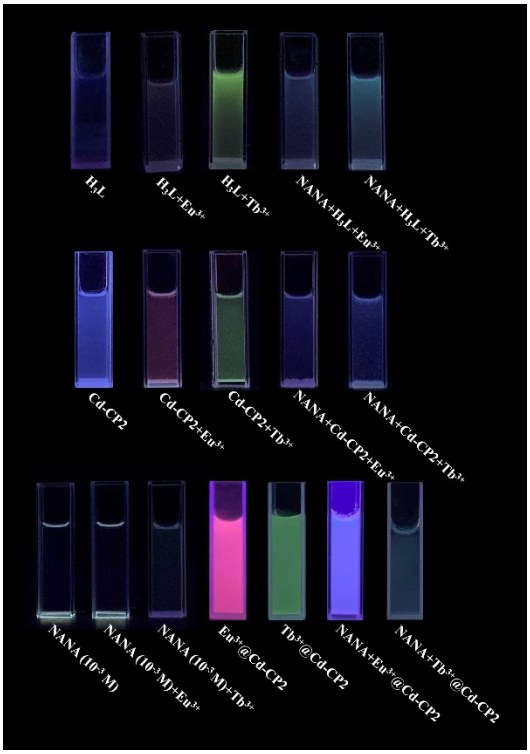

Fig. S41. Photos of the mixture of H_3L, **Cd-CP2** and Eu^{3+} or Tb^{3+} as well as **Eu^{3+}@Cd-CP2** and **Tb^{3+}@Cd-CP2** with or without NANA (10^{-3} M) under 254 nm UV light.